Cell Reports

Article

Biochemical and structural characterization of enzymes in the 4-hydroxybenzoate catabolic pathway of lignin-degrading white-rot fungi

Graphical abstract

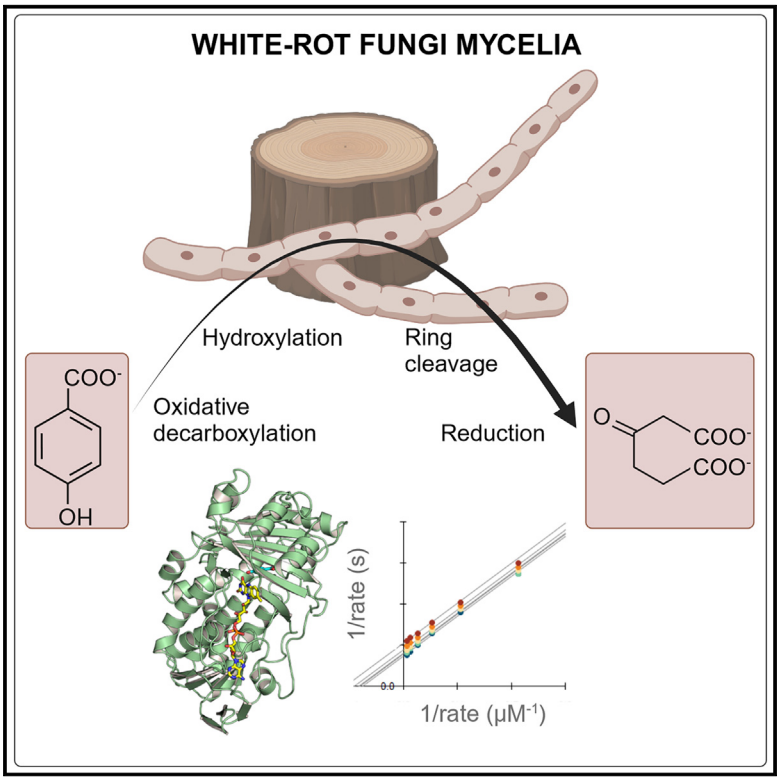

Authors

Eugene Kuatsjah, Alexa Schwartz, Michael Zahn, ..., Paul A. Cox, Andrew R. Pickford, Davinia Salvachúa

Correspondence

davinia.salvachua@nrel.gov

In brief

Kuatsjah et al. biochemically and structurally characterize enzymes in the 4-hydroxybenzoate catabolic pathway of white-rot fungi. Their findings advance the understanding of aromatic catabolism in fungi and reveal pathways and enzymes that convert lignin-derived compounds into valuable biochemicals, such as β-ketoadipate.

Highlights

- We characterize enzymes in the 4-hydroxybenzoate catabolic pathway of white-rot fungi
- We identify mechanistic differences between bacterial and fungal structural homologs
- We expand our understanding of monomeric aromatic compound catabolism by white-rot fungi
- We establish an enzymatic strategy to convert lignin-related compounds to β-ketoadipate

Kuatsjah et al., 2024, Cell Reports *43*, 115002
December 24, 2024
https://doi.org/10.1016/j.celrep.2024.115002

CellPress

Cell Reports

CellPress
OPEN ACCESS

Article

Biochemical and structural characterization of enzymes in the 4-hydroxybenzoate catabolic pathway of lignin-degrading white-rot fungi

Eugene Kuatsjah,[1,4] Alexa Schwartz,[1,2] Michael Zahn,[3,5] Konstantinos Tornesakis,[3] Zoe A. Kellermyer,[1] Morgan A. Ingraham,[1] Sean P. Woodworth,[1] Kelsey J. Ramirez,[1] Paul A. Cox,[3] Andrew R. Pickford,[3] and Davinia Salvachúa[1,6,*]

[1]Renewable Resources and Enabling Sciences Center, National Renewable Energy Laboratory, Golden, CO 80401, USA
[2]Advanced Energy Systems Graduate Program, Colorado School of Mines, Golden, CO 80401, USA
[3]Centre for Enzyme Innovation, School of the Environment and Life Sciences, University of Portsmouth, PO1 2DT Portsmouth, UK
[4]Present address: Institute of Sustainability for Chemicals, Energy and Environment (ISCE2), Agency for Science, Technology and Research (A*STAR), Singapore 138665, Republic of Singapore
[5]Present address: Biozentrum, Martin Luther University Halle-Wittenberg, 06120 Halle, Germany
[6]Lead contact
*Correspondence: davinia.salvachua@nrel.gov
https://doi.org/10.1016/j.celrep.2024.115002

SUMMARY

White-rot fungi (WRF) are the most efficient lignin-degrading organisms in nature. However, their capacity to use lignin-related aromatic compounds, such as 4-hydroxybenzoate, as carbon sources has only been described recently. Previously, the hydroxyquinol pathway was proposed for the bioconversion of these compounds in fungi, but gene- and structure-function relationships of the full enzymatic pathway remain uncharacterized in any single fungal species. Here, we characterize seven enzymes from two WRF, *Trametes versicolor* and *Gelatoporia subvermispora*, which constitute a four-enzyme cascade from 4-hydroxybenzoate to β-ketoadipate via the hydroxyquinol pathway. Furthermore, we solve the crystal structure of four of these enzymes and identify mechanistic differences with the closest bacterial and fungal structural homologs. Overall, this research expands our understanding of aromatic catabolism by WRF and establishes an alternative strategy for the conversion of lignin-related compounds to the valuable molecule β-ketoadipate, contributing to the development of biological processes for lignin valorization.

INTRODUCTION

White-rot fungi (WRF) are key organisms in global carbon cycling due to their ability to effectively degrade lignin, a heterogeneous aromatic polymer in plants and the second most abundant reservoir of organic carbon in nature.[1,2] The degradation of lignin begins with the secretion of a suite of extracellular enzymes by WRF, leading to the production of smaller components, such as aromatic monomers and oligomers.[3–5] WRF can completely mineralize lignin to carbon dioxide and water,[6] and this process has been traditionally associated with extracellular enzymatic processes.[7] However, in a recent study, we used systems biology and ^{13}C isotope labeling approaches in two WRF, *Trametes versicolor* and *Gelatoporia* (*Ceriporiopsis*) *subvermispora*, to confirm the utilization of lignin-related compounds as carbon sources.[8] From these results, we proposed the hydroxyquinol catabolic pathway for the intracellular conversion of 4-hydroxybenzoate (4HBA) toward central carbon metabolism, along with the potential enzymes involved in this conversion process.[8] 4HBA is derived from H-type lignin and is a monomeric phenol released from various bioenergy crops[9–11] as well as a typical intermediate of *p*-coumarate catabolism in bacteria.[12] Lignin also contains G- and S-type units (e.g., vanillate and syringate, respectively), which differ in the degree of methoxylation.[2] However, the catabolic pathways for G- and S-type units have not been fully elucidated in WRF.

The β-ketoadipate (βKA) pathway is a common and well-documented route for bacterial aerobic catabolism of 4HBA[12,13] (Figure 1A) and other lignin-related compounds derived from G-type lignin in bacteria.[12] Alternatively, 4HBA catabolism to βKA may also occur via the hydroxyquinol pathway, which has been reported and partially characterized in only a few microbes.[8,14–18] *Candida parapsilosis,* a nosocomial pathogenic yeast with limited association with lignin degradation,[19] has been the primary fungus studied for 4HBA catabolism in the hydroxyquinol pathway thus far.[15,20,21] In this yeast, the first step in the hydroxyquinol pathway is the oxidative decarboxylation of 4HBA to hydroquinone, catalyzed by a 4HBA 1-hydroxylase flavoprotein monooxygenase (FPMO) named MNX1 (Figure 1A).[20] Next, hydroquinone is hydroxylated by a different FPMO (named MNX3) to yield hydroxyquinol.[21] However, the subsequent reactions toward central carbon metabolism were proposed but not

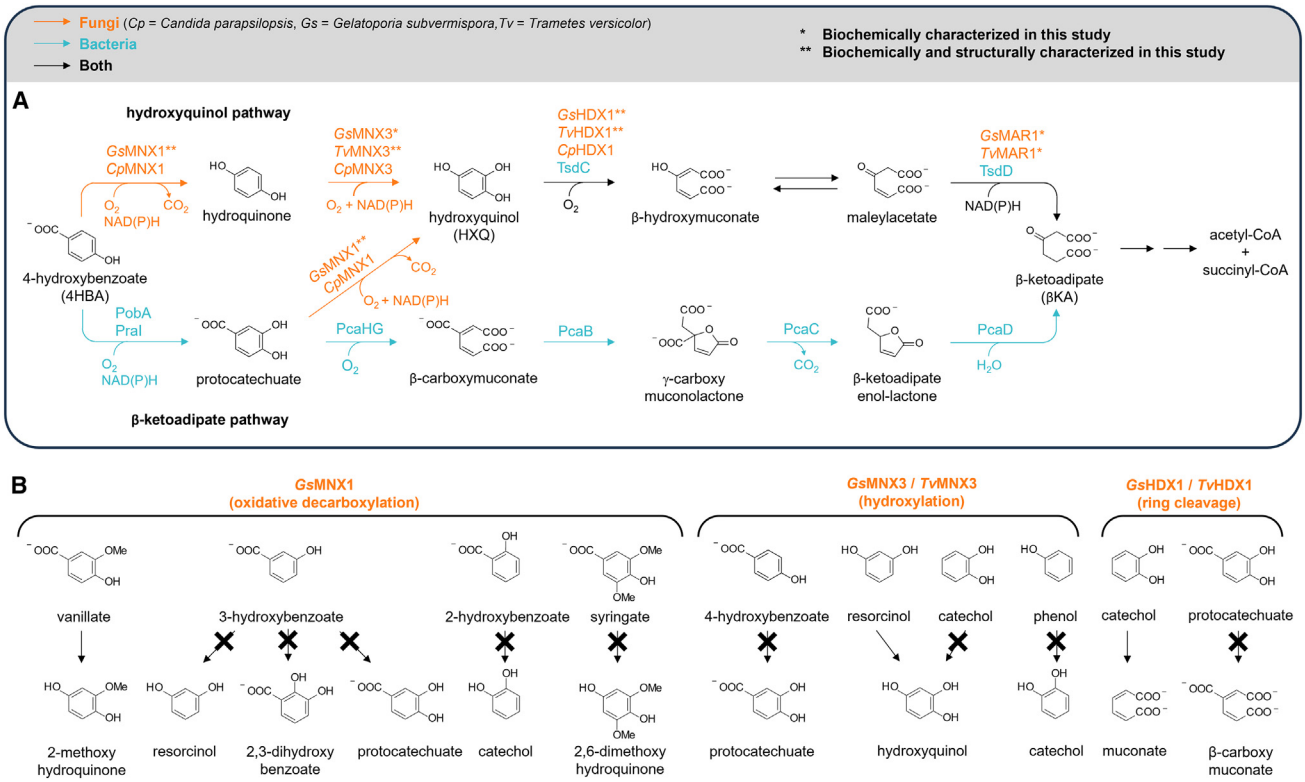

Figure 1. Pathways for aerobic conversion of 4HBA via the hydroxyquinol pathway and the conventional βKA pathway and other biochemical reactions tested in this study

(A) The hydroxyquinol pathway (top) includes representative fungal enzymes from *C. parapsilopsis* (*Cp*), *G. subvermispora* (*Gs*), and *T. versicolor* (*Tv*). MNX1, 4-hydroxybenzoate1-hydroxylase (decarboxylating); MNX3, hydroquinone 2-hydroxylase; HDX1, hydroxyquinol 1,2-dioxygenase (intradiol); MAR1, maleylacetate reductase. The hydroxyquinol pathway also includes representative bacterial enzymes from *R. jostii* RHA1. TsdC, hydroxyquinol 1,2-dioxygenase (intradiol); TsdD, maleylacetate reductase. The βKA pathway (bottom) includes representative bacterial enzymes from *P. putida* KT2440 and *Paenibacillus* sp. JJ-1b. PobA, 4HB3H; PcaHG, protocatechuate 3,4-dioxygenase (intradiol); PcaB, β-carboxymuconate lactonase; PcaB, γ-carboxymuconolactone decarboxylase; PcaD, βKA enol-lactonase; PraI, 4HB3H.

(B) Additional biochemical reactions tested in this study with *Gs*MNX1, *Gs*MNX3, *Tv*MNX3, *Gs*HDX1, and *Tv*HDX1. The x over the arrows indicates the absence of activity on that specific molecule.

identified in this yeast.[15] Specifically, these reactions were proposed to involve *ortho*-ring opening of hydroxyquinol by a non-heme iron-dependent dioxygenase (named HDX1) to produce 3-hydroxy-*cis*,*cis*-muconate, which abiotically tautomerizes with maleylacetate (Figure 1A). Last, maleylacetate could be reduced by a maleylacetate reductase (named MAR1) to produce βKA, which can enter central carbon metabolism (Figure 1A).

The reduction from maleylacetate to βKA has not yet been identified or characterized in the fungal kingdom.[22] In contrast, this reduction step has been studied in bacteria for the catabolism of γ-resorcylate and *p*-nitrophenol.[16–18] Namely, the catabolism of γ-resorcylate by *Rhodococcus jostii* RHA1, a bacterium well known for its ability to catabolize aromatic compounds, involves both the hydroxyquinol dioxygenase (*Rj*TsdC) and MAR1 (*Rj*TsdD).[18] However, *R. jostii* RHA1 lacks the additional upstream enzymes of the hydroxyquinol pathway (i.e., MNX1 and MNX3) for the catabolism of 4HBA (Figure 1A).[18] Enzymes homologous to MNX3 and HDX1 have been also been biochemically characterized recently in the fungus *Phanerochaete chrysosporium*,[23–25] but, to our knowledge, the ability of this fungus to utilize aromatic compounds (e.g., 4HBA) as carbon sources has yet to be reported. Regardless of their origin, whether bacterial or fungal, there is currently a lack of structure-function information regarding key enzymes in the hydroxyquinol pathway. Such characterization will be essential to understand this pathway and how it is different from those in the canonical βKA pathway.

Here, we report the characterization of seven enzymes from WRF: four constituting the entire hydroxyquinol pathway from *G. subvermispora* and three from *T. versicolor*. In addition, we included two enzymes from *R. jostii* RHA1 for direct comparison (Figure 1). This work encompasses comprehensive biochemical characterization, including product identification, kinetically determined substrate specificities, and structural biology. Taken together, this work contributes to our collective understanding of intracellular aromatic catabolic pathways in WRF and pinpoints mechanistic differences between fungal and bacterial systems for these transformations. Additionally, the knowledge gained from this study could be applied to enzyme- or microbe-based technologies for converting

lignin-derived aromatic compounds into valuable products such as βKA, thus contributing to enhancing the overall feasibility of lignocellulosic biorefineries.[26–28]

RESULTS

*Gs*MNX1 oxidatively decarboxylates 4HBA, protocatechuate, and vanillate

The first biochemical reaction proposed in the hydroxyquinol pathway of WRF is the MNX1-catalyzed oxidative decarboxylation of 4HBA to hydroquinone (4HBA 1-hydroxylase activity) (Figure 1A). Prior *in silico* analyses identified a set of MNX1 homologs in both *T. versicolor* (TRAVEDRAFT_32834 and TRAVEDRAFT_175239) and *G. subvermispora* (CERSUDRAFT_120062, CERSUDRAFT_119636, and CERSUDRAFT_90429).[8] Among these, three proteins (TRAVEDRAFT_32834, CERSUDRAFT_120062, and CERSUDRAFT_90429) were produced solubly using the *Escherichia coli* heterologous expression host.[8] The first two proteins showed significant nicotinamide adenine dinucleotide phosphate (NAD[P]H) turnover in the presence of either 4HBA or protocatechuate, whereas the latter showed negligible turnover,[8] and thus, CERSUDRAFT_90429 was not investigated further. Here, the ability of the other two putative MNX1 enzymes to decarboxylate 4HBA and protocatechuate was evaluated by a high-performance liquid chromatography (HPLC)-based method. Notably, TRAVEDRAFT_32834 was unable to transform either substrate tested, which suggests that the consumption of NAD(P)H reported previously[8] was due to futile cycling (Figure S1A). In contrast, CERSUDRAFT_120062 (hereafter called *Gs*MNX1) is active on both substrates (Figures 1A and S1B). Therefore, *Gs*MNX1 was selected for additional biochemical and structural analyses.

To explore the substrate specificity of *Gs*MNX1, we screened its activity against 2-hydroxybenzoate and 3-hydroxybenzoate (which have carboxy and hydroxy groups in variable positions relative to 4HBA), vanillate (a G-type lignin-related compound[8] and an intermediate of ferulate catabolism in some microbes[29]), and syringate (an S-type lignin-related compound[8]) (Figure 1B), with 4HBA and protocatechuate used as positive controls, via an HPLC method. Conversions were only observed for 4HBA, protocatechuate, and vanillate to produce hydroquinone, hydroxyquinol, and 2-methoxyhydroquinone, respectively (Figures 1A, 1B, and S1). Next, we studied the potential extent of reaction uncoupling (futile cycling) in *Gs*MNX1 by comparing the rates of oxygen consumption in the presence or absence of catalase by oxygraphy. Reaction uncoupling in this study is defined as the consumption of O_2 and reducing equivalent without a concomitant oxidative decarboxylation of the phenolic substrate, which may occur when the oxygenase, or its redox components, encounters unsuitable substrates. This abrupt reduction of O_2 typically produces H_2O_2, which is readily converted by catalase to H_2O and ½ O_2; this phenomenon effectively decreases the total oxygen consumption up to half for complete reaction uncoupling. In these experiments, no rate changes were observed in the *Gs*MNX1-catalyzed hydroxylation of 4HBA, protocatechuate, or vanillate, indicating that these reactions are coupled efficiently (Figure S2).

Regarding cofactors, in this system, NAD(P)H functions as a universal intracellular redox intermediary, although some enzymes exhibit a preference for a specific form of the cofactor, which can be loosely associated with catabolic and anabolic processes. On the other hand, the flavo-coenzyme acts as a redox-active prosthetic group in the FPMO, mediating the oxidation of the organic substrate. The FPMO catalytic cycle involves reductive and oxidative half-reactions. In the reductive half-reaction, the flavo-coenzyme (flavin adenine dinucleotide [FAD] or flavin mononucleotide [FMN]) is reduced at the expense of the nicotinamide cofactor (NAD(P)H), which, in turn, reacts with an O_2 species to form the reactive flavoperoxo intermediate, enabling the subsequent oxidation of the organic substrate.[30,31] Both nicotinamide adenine dinucleotide plus hydrogen NADH and NADPH were utilized as reducing equivalents by *Gs*MNX1; however, NADPH is highly favored and is likely the physiological cofactor, as indicated by a lower Michaelis-Menten constant by at least an order of magnitude when compared to NADH (Table 1; Figure S3). The cofactor preference for FPMO has been described in greater detail elsewhere.[32] In short, this preference is linked to the residue composition at the opening of the active site, which includes a specific consensus sequence that biases the preference toward NADH or NADPH. Moreover, this bias correlates with the life cycle of the host microbes, with faster- and slower-growing species favoring NADPH and NADH, respectively. *Gs*MNX1 exhibits Michaelis-Menten behavior with the following catalytic efficiency: protocatechuate > 4HBA > vanillate, which is the same substrate preference order as *Cp*MNX1. Nevertheless, the catalytic efficiency of *Gs*MNX1 is an order of magnitude higher than that of *Cp*MNX1 toward protocatechuate (Table 1).

The active center of *Gs*MNX1 exhibits structural similarity to hydroxylases, but *Gs*MNX1 does not catalyze hydroxylation without decarboxylation

MNX1 comprises a single FAD oxidoreductase domain (PF01494).[33] To gain a better understanding of its catalytic machinery, we solved the crystal structure of *Gs*MNX1 with diffraction data extending to a resolution of 1.82 Å with a bound coenzyme FAD in the closed conformation (Figure 2A). The mobility of FAD is a well-documented phenomenon within the catalytic cycle of FPMO, with the open or closed FAD conformations defined as the position of the isoalloxazine moiety facing away or toward the aromatic substrate, respectively.[34,35] The open conformation is associated with the reductive half-reaction, where the solvent-facing flavin is reduced by NAD(P)H. The closed conformation relates to the reduced flavin, which reacts with O_2 to perform the oxidative half-reaction. The overall structure of *Gs*MNX1 matches the typical architecture of FPMO, and the closest structural homologs in the PDB are from bacteria; namely, the 3-hydroxybenzoate 6-hydroxylase (3HB6H) from *R. jostii* RHA1 (PDB: 4BK1; 32% sequence identity, a root-mean-square deviation [RMSD] value of 2.0 Å over 377 residues aligned)[36] and the 6-hydroxynicotinic acid 3-monooxygenase (NicC) from *P. putida* KT2440 (PDB: 5EOW; 32% sequence identity, RMSD value of 2.0 Å over 343 residues aligned).[37]

Our attempt to obtain the substrate-bound structure either by co-crystallization or soaking methods was not successful.

Table 1. Steady-state kinetic parameters of enzymes evaluated in this study and biochemically characterized previously

Enzyme function	Substrate	Enzyme	k_{cat}^{app} s^{-1}	K_M^{app} μM	k_{cat}^{app}/K_M^{app} s^{-1} μM^{-1}	$K_M^{app}{}_{NADH}$ μM	$K_M^{app}{}_{NADPH}$ μM	$K_{iu\ 4HBA}$ mM	Reference
4-hydroxybenzoate-1-decarboxylase (decarboxylating)	4HBA	*Gs*MNX1	1.3 ± 0.1	7.4 ± 0.3	0.18 ± 0.01	>10,000	200 ± 7	NI	this study
		*Cp*MNX1[a]	10	10	1	19	169	NI	Eppink et al.[20]
	vanillate	*Gs*MNX1	2.0 ± 0.5	38.5 ± 0.2	0.05 ± 0.01	NI	NI	NI	this study
		*Cp*MNX1	11.8	125	0.1	NI	NI	NI	Eppink et al.[20]
	protocatechuate	*Gs*MNX1	4.4 ± 0.7	0.2 ± 0.04	22 ± 4	NI	NI	NI	this study
		*Cp*MNX1	16.8	9	2	NI	NI	NI	Eppink et al.[20]
Hydroquinone-2-hydroxylase	hydroquinone	*Tv*MNX3	6.8 ± 0.1	13 ± 1	0.52 ± 0.04	NI	54 ± 3	4.6 ± 0.3	this study
		*Gs*MNX3	3.2 ± 0.2	11 ± 1	0.29 ± 0.03	NI	22 ± 1	17 ± 6	this study
		*Pc*MNX3[b]	1.8 ± 0.2	48 ± 8	0.036 ± 0.007	NI	90 ± 20	N/A	Suzuki 2023[23]
		*Cp*MNX3[c]	5.8 ± 0.6	1.0 ± 0.1	5.8 ± 0.8	NI	18 ± 2	N/A	Eppink et al.[21]
	resorcinol	*Tv*MNX3	2.1 ± 0.1	70 ± 10	0.030 ± 0.005	NI	NI	NI	this study
		*Gs*MNX3	0.85 ± 0.03	34 ± 4	0.025 ± 0.003	NI	NI	NI	this study
		*Pc*MNX3[b]	N/A	N/A	N/A	NI	NI	NI	Suzuki 2023[23]
		*Cp*MNX3[c]	2.5 ± 0.3	25 ± 3	0.10 ± 0.01	NI	NI	NI	Eppink et al.[21]
Hydroxyquinol 1,2-dioxygenase (intradiol)	hydroxyquinol	*Rj*TsdC	48 ± 1	14 ± 1	3.4 ± 0.3	NI	NI	NI	this study
		*Tv*HDX1	19.1 ± 0.3	7.2 ± 0.4	2.7 ± 0.2	NI	NI	NI	this study
		*Gs*HDX1	19.5 ± 0.4	8.1 ± 0.5	2.4 ± 0.2	NI	NI	NI	this study
		*Pc*HDX1[d]	23 ± 4	37 ± 9	0.6 ± 0.2	NI	NI	NI	Kato 2022[25]
	catechol	*Rj*TsdC	0.30 ± 0.01	19.4 ± 0.1	0.016 ± 0.001	NI	NI	NI	this study
		*Tv*HDX1	0.30 ± 0.01	6.3 ± 0.4	0.048 ± 0.003	NI	NI	NI	this study
		*Gs*HDX1	0.12 ± 0.01	3.6 ± 0.3	0.033 ± 0.003	NI	NI	NI	this study
		*Pc*HDX1[d]	0.16 ± 0.01	6.2 ± 0.9	0.026 ± 0.002	NI	NI	NI	Kato 2022[25]
Maleylacetate reductase	maleylacetate	*Rj*TsdD	400 ± 10	45 ± 2	9.0 ± 0.4	56 ± 1	52 ± 2	NI	this study
		*Tv*MAR1	50 ± 1	40 ± 1	1.3 ± 0.1	480 ± 20	19 ± 1	NI	this study
		*Gs*MAR1	23.0 ± 0.8	15.7 ± 0.2	1.4 ± 0.1	740 ± 50	5.2 ± 0.3	NI	this study

Experiments for MNX1, MNX3, HDX1, and *Rj*TsdC were performed following the consumption of O_2 in air-saturated 50 mM Tris.SO_4 (pH 7.0) at 25°C. Reaction assays for MNX1 and MNX3 were further supplemented with 10 μM FAD. Experiments for MAR1 and TsdD were performed spectrophotometrically following the depletion of NAD(P)H in air-saturated 50 mM Tris.SO_4 (pH 7.0) at 25°C. Assays were conducted with $n \geq 15$, and errors show the error from the fittings. 4HBA, 4-hydroxybenzoate. NI indicates parameters that were not investigated in this study.

[a]Assay conditions for *Cp*MNX1. The activity was monitored polarographically via O_2 consumption at 25°C in air-saturated 50 mM potassium phosphate (pH 7.6), 10 μM FAD, ≤0.5 mM aromatic substrate, and 0.2 mM NADH.

[b]Assay conditions for *Pc*MNX3. The activity was monitored spectrophotometrically following NADPH oxidation at 37°C in air-saturated 50 mM HEPES (pH 7.5), ≤0.6 M aromatic substrate, and 0.2 mM NADPH.

[c]Assay conditions for *Cp*MNX3. The activity was monitored polarographically via O_2 consumption at 25°C in air-saturated 50 mm potassium phosphate (pH 7.6), 10 μm FAD, ≤1 mM phenolic substrate, and ≤0.4 mm NADPH.

[d]Assay conditions for *Pc*HDX1. The activity was monitored polarographically via O_2 consumption at 30°C in air-saturated 50 mm 2-(N-morpholino)ethanesulfonic acid (pH 6.0), ≤0.6 mM phenolic substrate, ≤0.4 mm NADPH, and 6 μg superoxide dismutase.

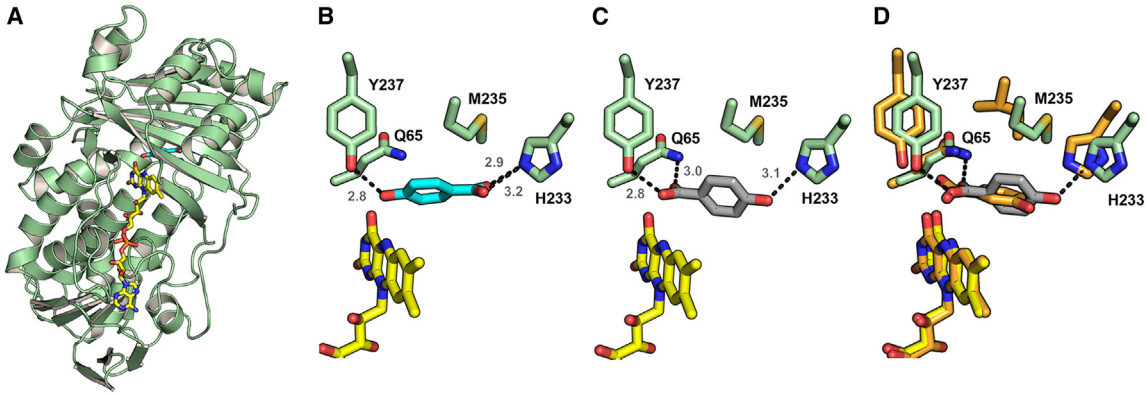

Figure 2. *Gs*MNX1 structure

(A) Crystal structure of *Gs*MNX1 with bound coenzyme FAD (yellow carbon atoms) and docked substrate 4HBA (cyan carbons).

(B) Magnification of the active site—docking mode_1 (4HBA in cyan). The interatomic distances shown are in Å.

(C) Docking mode_2 (4HBA in gray).

(D) Superposition of the active sites of *Gs*MNX1 (green) with docked substrate 4HBA and 3HB6H from *R. jostii* RHA1 with bound substrate 3-hydroxybenzoate (PDB: 4BK1, orange). The latter structure was solved for the H213S mutant; therefore, PDB: 4BJZ was used to visualize His213.

Therefore, we docked the substrate 4HBA into the active site of *Gs*MNX1 and found two possible binding orientations with similar free energy scores. There are no explicit steric or polar determinants present for the positions *ortho* to the phenolic group of the substrate in either of our docked models. In the first model (Figure 2B; −5.162 kcal/mol), the phenolic group of 4HBA is coordinated by Tyr237. This model resembles the docked model for NicC from *P. putida* KT2440, where the phenol-interacting tyrosine is proposed to act as a base catalyst that deprotonates the phenolic group of the substrate to yield a dearomatized quinoid intermediate that precedes oxidative decarboxylation.[37,38] The second model (Figure 2C; −4.872 kcal/mol) has 4HBA bound in a "flipped" orientation relative to the first model, where the phenolic group of 4HBA is coordinated by His233. This latter model matches closely the substrate binding orientation found in the crystal structure of 3HB6H (PDB: 4BK1) from *R. jostii* RHA1.[36] Despite the good superposition between 4HBA from our docked structure and 3-hydroxybenzoate from the 3HB6H enzyme-substrate complex (PDB: 4BK1; Figure 2D), *Gs*MNX1 is unable to hydroxylate 3-hydroxybenzoate (Figures 1B and S1). No phospholipid was found in the *Gs*MNX1 crystal structure, unlike the 3HB6H structure (PDB: 4BK1), where the lipid tail reaches the enzyme active site and is partly implicated in the proper substrate positioning.[36] Together, these models underscore the diverse reactions catalyzed by FPMO enzymes and, especially in the context of *Gs*MNX1, highlight the importance of polar interactions between the substrate and the active-site residues to facilitate the Tyr- or His-catalyzed substrate dearomatization for the oxidative C–C bond fission (Figure S4).

*Gs*MNX3 and *Tv*MNX3 catalyze the hydroxylation of hydroquinone and resorcinol and exhibit futile cycling with catechol and phenol

The second step proposed in the hydroxyquinol pathway involves the hydroxylation of hydroquinone at the *ortho* position to produce hydroxyquinol, which primes the benzene ring with a vicinal diol moiety for the ensuing oxygenative ring fission (Figure 1A). This process has been suggested to be catalyzed by the FPMO, MNX3 from *T. versicolor* (TRAVEDRAFT_58730) and *G. subvermispora* (CERSUDRAFT_82057) (hereafter called *Tv*MNX3 and *Gs*MNX3, respectively).[8] Like *Gs*MNX1, purified protein preparations of *Tv*MNX3 and *Gs*MNX3 are yellow in color, consistent with a significant incorporation of FAD coenzyme. Notably, the MNX3 from WRF is not subject to auto-truncation upon purification like MNX3 from *C. parapsilosis* (hereafter called *Cp*MNX3).[21] In an HPLC-based assay, *Tv*MNX3 and *Gs*MNX3 were confirmed to transform hydroquinone to hydroxyquinol (Figure S5), and they were shown to not turn over 4HBA or protocatechuate under the conditions tested (Figure 1B). This contrasts prior reports on MNX3 from *P. chrysosporium* (hereafter called *Pc*MNX3), which hydroxylates 4HBA, albeit at a very low efficiency.[23]

To evaluate the versatility of *Tv*MNX3 and *Gs*MNX3 against phenolic compounds of varying degrees and positioning of the hydroxylation, we also evaluated the reactivity of these enzymes against phenol, catechol, and resorcinol (Figure 1B). O_2 consumption was observed for all compounds tested. However, the presence of catalase, used to evaluate reaction uncoupling, halved the observed rates of *Tv*MNX3- and *Gs*MNX3-catalyzed reactions in the presence of catechol and phenol, which implies a complete reaction uncoupling as an equimolar amount of H_2O_2 was produced for every mol of O_2 and NADPH consumed (Figure S6). Conversely, no rate changes in the presence of catalase were observed when *Tv*MNX3 and *Gs*MNX3 reacted with hydroquinone and resorcinol, indicating no reaction uncoupling. Conversely, *Cp*MNX3 has been shown to hydroxylate phenol and catechol with little to no uncoupling.[21]

*Tv*MNX3 and *Gs*MNX3 displayed Michaelis-Menten behavior for hydroquinone and resorcinol, and the steady-state kinetic parameters are summarized in Table 1. The catalytic efficiencies of *Tv*MNX3 and *Gs*MNX3 are comparable with respect to hydroquinone and resorcinol, although *Gs*MNX3 operates under half the Michaelis-Menten constant when compared to *Tv*MNX3. Catalytic efficiency comparison between different biochemically

characterized MNX3 ranks as follows: *Cp*MNX3 > *Tv*MNX3 ≈ *Gs*MNX3 > MNX3 from *P. chrysosporium* (*Pc*MNX3) (Table 1).[21,23] The higher activity from *Cp*MNX3 may be partly attributable to the different protein production methodologies. *Cp*MNX3 was produced natively in *C. parapsilosis*, while MNX3 from WRF was produced heterologously in *E. coli*.[21,23] In all instances, the purified MNX3 enzymes exhibited a strict nicotinamide cofactor preference for NADPH and were minimally reactive with NADH (Figure S7).[21,23] We note that *Cp*MNX3 was susceptible to substrate inhibition by hydroquinone and resorcinol,[21] whereas no substrate inhibition was observed for either *Tv*MNX3 or *Gs*MNX3 under the range of substrate concentrations tested (≤75 μM). This result indicates the robustness of these fungal enzymes in the presence of aromatic compounds.

MNX1 C_1 oxidative decarboxylation precedes MNX3 C_3 hydroxylation in the aromatic ring

To confirm the sequence of the reactions catalyzed by MNX1 and MNX3 and identify potential inhibitions in these initial steps, we analyzed the reaction inhibition profile of MNX3 by monitoring its reactivity toward aromatic substrates and products of MNX1 and comparing the rates of *Tv*MNX3- and *Gs*MNX3-catalyzed hydroxylation of hydroquinone in the presence of 4HBA, protocatechuate, vanillate, and 2-methoxyhydroquinone. The initial velocity of MNX3-catalyzed hydroquinone hydroxylation was lower (up to ~0.5 times lower) in the presence of 4HBA, protocatechuate, and vanillate but not 2-methoxyhydroquinone, suggesting that these compounds are inhibitory (Figure S8). In contrast, the presence of hydroquinone did not lower the rate of *Gs*MNX1-catalyzed oxidative decarboxylation of 4HBA (Figure S9). We further explored the nature of inhibition of 4HBA toward the hydroquinone hydroxylation rate of *Gs*MNX3 and *Tv*MNX3, as 4HBA is the most inhibitory compound of the species tested. 4HBA acts as a modest uncompetitive inhibitor, as indicated by parallel fitting lines in the Lineweaver-Burk plot (Table 1; Figure S10). Based on the substrate specificities reported previously for both enzymes (Table 1) and the inhibitory nature of MNX1 substrates toward *Tv*MNX3 and *Gs*MNX3, this reinforces that MNX1-catalyzed oxidative decarboxylation of 4HBA precedes MNX3-catalyzed hydroxylation.

*Tv*MNX3 showcases a distinctive thioredoxin domain and activity compared to closely related bacterial and fungal structural homologs

MNX3 harbors two distinct domains, an N-terminal FAD binding domain (PF01494) and a C-terminal phenol hydroxylase dimerization domain (PF07976/cd02979), which have also been described as a thioredoxin-like superfamily.[33] To provide insights into the basis of substrate specificity of *Tv*MNX3 and *Gs*MNX3, we sought to determine their molecular structures. We solved the holo-structure of *Tv*MNX3, which included bound coenzyme FAD in an open conformation with diffraction data extending to a resolution of 2.4 Å, but that of *Gs*MNX3 proved elusive. We docked the substrate hydroquinone into the active site for a more complete model (Figure 3A). *Tv*MNX3 forms a dimer with a single FAD molecule bound in each subunit, both built in the open conformation. The FAD molecule is strongly bound in one subunit and more loosely in the other. The loose association of FAD within FPMO has been reported previously; therefore, it requires FAD supplementation in the kinetics assay buffer.[32] The active site reveals a network of hydrogen bonding surrounding the aromatic substrate that exhibits one hydroxyl group of hydroquinone forming hydrogen bonds with Asp53 and Tyr252, whereas the opposite hydroxyl group interacts with Glu112 and Lys229 (Figure 3B). The latter is substituted with an arginine in *Pc*MNX3 and *Cp*MNX3. The closest structural homolog of *Tv*MNX3 is a phenol hydroxylase from the yeast *Trichosporon cutaneum* (PDB: 1FOH) with 44% sequence identity. Both structures form a dimer, and the monomers superimpose one another well with an RMSD value of 1.40 Å over 539 residues aligned (Figure 3C). The difference in FAD conformation in FPMO does not appear to affect substrate binding or active-site residue conformations (Figure 3D), as shown in the phenol hydroxylase structure, which harbors FAD in differing conformations in each of their subunits. However, it is worth noting that *Tv*MNX3 did not exhibit activity on phenol (Figure 1B), in contrast to the reported activity in *T. cutaneum*.

*Tv*MNX3 harbors a C-terminal thioredoxin domain, but its role is unclear. Thioredoxins contain redox-active disulfide bridges and may serve as an additional redox active site or to maintain overall protein stability.[39,40] Its function, however, can be inferred from its annotation as a dimerization domain. Indeed, only one pair of residues (Glu70 and Arg74) contributing to the dimer interface is solely from the FPMO domain, whereas the remaining 15 residues are from or interacting with the thioredoxin domain (Figure S11).[41] It is possible for an FPMO lacking a thioredoxin domain to still form a dimeric structure, as evidenced by our recent structure of 4HBA 3-hydroxylase (4HB3H, PraI; PDB: 7ON9).[42] The monomer of *Tv*MNX3 and PraI superimpose well with an RMSD value of 2.27 Å (343 residues aligned) despite the low sequence identity of 16% and the different contact angles between the subunits leading to different quaternary structure configuration (Figures 3E and 3F). Nevertheless, the purified *Tv*MNX3 used in this study harbors a C-terminal poly-His tag and adopts a monomeric quaternary structure when evaluated using size-exclusion chromatography under the condition tested (Figure S12). The poly-His tag or the buffer used may prevent dimerization, and this protein may indeed form higher oligomers *in vivo*. Altogether, these results again highlight the plasticity of the FPMO protein scaffold and the myriad reactions it catalyzes.

Comparison with other characterized FPMOs suggests a common mechanism within the FPMO *ortho*-phenol hydroxylases, as highlighted by the common structural fold and catalytic machinery. The sequence identities of known fungal MNX3 enzymes range from 40%70%, and the RMSD values of the AlphaFold models of *Gs*MNX3, *Cp*MNX3, and *Pc*MNX3 are ≤1.41 Å (≥568 aligned residues) compared to *Tv*MNX3. With this common architecture, these enzymes may be expected to function similarly, especially with full conservation of the substrate-coordinating residues. With the aim to compare it with bacterial FPMOs, a functional homolog to MNX3 from *R. jostii* RHA1 was chosen, the resorcinol 6-hydroxylase TsdB (hereafter called *Rj*TsdB) from the γ-resorcylate catabolism.[18] Characterization of this potential bacterial counterpart to MNX3 was not successful (Text S1; Figure S13). Indeed, *Rj*TsdB diverges significantly from MNX3, and it shares ≤20% sequence identity while lacking

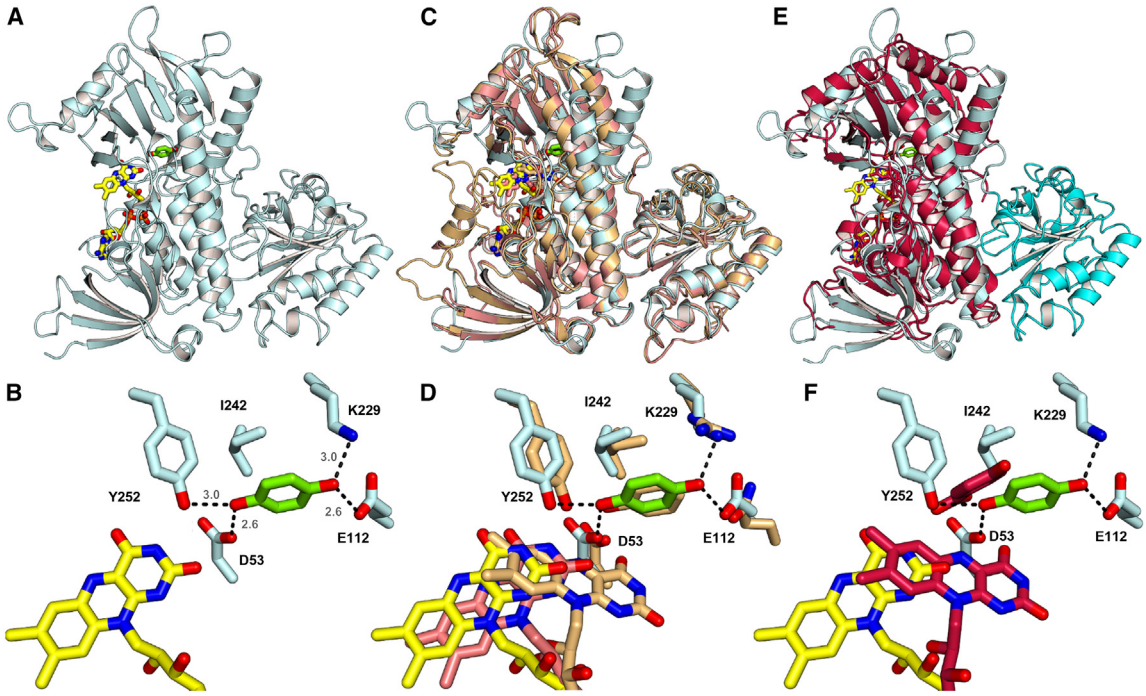

Figure 3. Structural architecture of *Tv*MNX3 and comparison with other FPMOs

(A) Crystal structure of *Tv*MNX3 with bound coenzyme FAD in the open conformation (yellow carbon atoms) and docked substrate hydroquinone (green carbons).

(B) Molecular interactions of the docked substrate hydroquinone (green) with the active-site residues of *Tv*MNX3 (blue) in the FAD open conformation (FAD in yellow). The interatomic distances shown are in Å.

(C) Superposition of an FAD open conformation (pink) and FAD closed conformation (tan) protein chain of phenol hydroxylase from *T. cutaneum* (both PDB: 1FOH) with *Tv*MNX3 (blue).

(D) Comparison of the different coenzyme FAD conformations of *Tv*MNX3 (open FAD in yellow) and phenol hydroxylase (open FAD in pink and closed FAD in tan). The active-site residues and the substrate phenol of the closed FAD conformation are shown and colored in tan. *Tv*MNX3 active-site residues are colored in blue and are labeled, and the docked hydroquinone is shown in green.

(E) Superposition of 4HB3H PraI (PDB: 7ON9) (red) with *Tv*MNX3 (blue). *Tv*MNX3 has a C-terminal thioredoxin-like domain (cyan) that is absent in PraI.

(F) Comparison of the FAD conformations of *Tv*MNX3 (open FAD in yellow) and PraI (closed FAD in red). The PraI substrate 4HBA is shown in red, and the hydroquinone docked to *Tv*MNX3 is shown in green.

all four active site residues identified previously in association with hydroquinone binding. A broader comparison of MNX3 to other characterized FPMOs revealed a specific functional clustering around phenol-2-monooxygenase activity, which represents the simplest common denominator substrate (Figure S14). Indeed, this cluster contains the dimeric phenol-2-monooxygenase from *T. cutaneum*.[43] Additionally, this cluster includes enzymes that hydroxylate para- and meta-hydroxybenzoates at the position *ortho* to the phenolic group to yield protocatechuate, which is distinct from the thioredoxin-less FPMOs, such as PobA and PraI (Figure 3).[42,44–46] In all instances, the *ortho*-phenol hydroxylation in FPMO may proceed by the deprotonation of the phenol, likely by the conserved tyrosine, which primes the alpha carbon to abstract a hydroxy group from the flavin hydroxyperoxide (Figure S15).[47,48]

The catalytic efficiency of fungal hydroxyquinol dioxygenases is comparable to that of their bacterial counterparts

The next suggested reaction in sequence in the hydroxyquinol pathway of WRF is the intradiol ring opening of hydroxyquinol as catalyzed by non-heme iron dioxygenases (Figure 1A). In this study, we evaluated three proposed hydroxyquinol dioxygenases from *T. versicolor* (TRAVEDRAFT_28066, *Tv*HDX1), *G. subvermispora* (CERSUDRAFT_116134, *Gs*HDX1), and TsdC from *R. jostii* RHA1 (ro01857, *Rj*TsdC) (Figure 1A).[8] Our plasmid-encoded *Tv*HDX1 bears an additional 33 amino acids at the N terminus that is derived from an earlier start codon that was not included in the subsequent GenBank entry; nevertheless, this addition does not seem to affect the overall protein folding and activity (*vide infra*). All three proteins were purified to homogeneity following a two-step aerobic purification protocol. The resulting protein preparations are reddish-brown in color, consistent with the metal-to-ligand charge transfer between ferric ion and tyrosine typical of intradiol dioxygenases.[49]

HPLC-based detection of hydroxyquinol dioxygenase activity is challenging due to the instability of hydroxyquinol and the lack of commercial sources of its putative product, maleylacetate (Figure 1). Hydroxyquinol readily oxidizes under aerobic aqueous conditions at pH 7, which complicates reaction monitoring via substrate depletion. Indeed, the ring-opened reaction products from these reactions are colorless, which is consistent with an

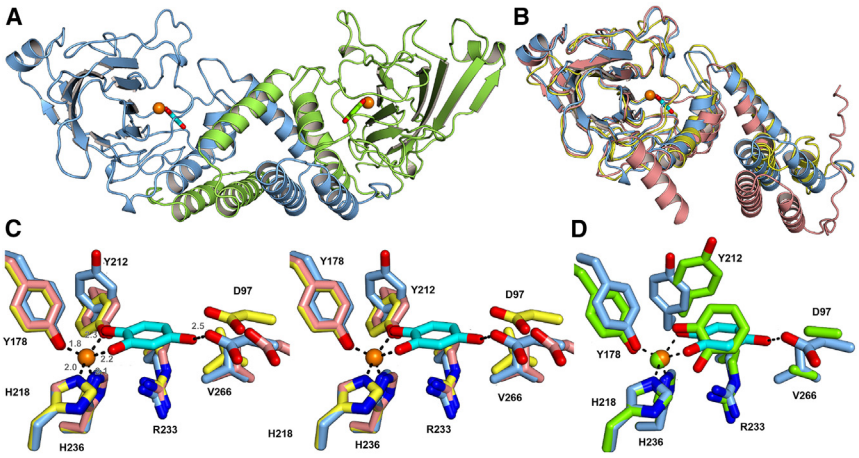

Figure 4. Structural architecture of *Tv*HDX1, *Gs*HDX1, and *Rj*TsdC

(A) Crystal structure of dimeric *Tv*HDX1 with bound ferric ions (orange) and docked substrate hydroxyquinol (cyan and green).

(B) Superposition of the monomeric structural units of *Tv*HDX1 (blue), *Gs*HDX1 (pink), and *Rj*TsdC (yellow).

(C) Stereo view of the active sites of *Tv*HDX1 (pale blue), *Gs*HDX1 (pink), and *Rj*TsdC (yellow). For *Tv*HDX1, the bound ferric ions (orange) and docked substrate hydroxyquinol (cyan) are shown as well as the residue labels. The interatomic distances shown are in Å.

(D) Superposition of *Tv*HDX1 with docked substrate hydroxyquinol (cyan) with the crystal structure of catechol-1,2-dioxygenase from *B. ambifaria* with bound catechol (green; PDB: 5VXT).

intra-diol (*ortho*) cleavage product, in contrast to the yellow-colored muconate semialdehyde structure from extra-diol (*meta*) cleavage products.[50] To confirm the production of maleylacetate from hydroxyquinol by ring-opening dioxygenases, we conducted a chain reaction that also included a previously characterized reductase, MAR1 (TsdD from *R. jostii* RHA1; hereafter called *Rj*TsdD)[18] (Figure 1A) to produce βKA, for which an HPLC-based quantification method is available.[51] A mixture containing 1 μM each of *Tv*HDX1, *Gs*HDX1, and *Rj*TsdC transformed hydroxyquinol to maleylacetate in an equimolar fashion (Figure S16A). To further explore their substrate specificities, we tested *Tv*HDX1, *Gs*HDX1, and *Rj*TsdC on other aromatic diols, including catechol and protocatechuate, by oxygraphy. Only catechol elicited significant O_2 consumption to produce muconate at near-stoichiometric amounts (Figure S16B).

The catalytic efficiencies of *Tv*HDX1, *Gs*HDX1, and *Rj*TsdC were determined by oxygraphy following the consumption of O_2 upon mixing with either hydroxyquinol or catechol. These dioxygenases are consistently most active against hydroxyquinol and minimally against catechol. *Tv*HDX1, *Gs*HDX1, and *Rj*TsdC exhibit Michaelis-Menten kinetic behavior for the cleavage of hydroxyquinol and catechol, as summarized in Table 1. The kinetic parameters for *Tv*HDX1 and *Gs*HDX1 against hydroxyquinol are at parity; conversely, *Rj*TsdC is ∼30% more efficient (as indicated by k_{cat}/K_M ratio) than the WRF HDX1. *Pc*HDX1 is ∼5-fold less efficient than *Tv*HDX1 and *Gs*HDX1 for hydroxyquinol, which is largely driven by an elevated Michaelis-Menten constant.

*Rj*TsdC exhibits greater structural similarity to *Gs*HDX1 and *Tv*HDX1 than the fungal enzymes do among themselves

To evaluate the structural architecture of these intradiol dioxygenases, the dimeric structures of fungal *Tv*HDX1 (Figure 4A), *Gs*HDX1, and bacterial *Rj*TsdC were solved by X-ray crystallography with diffraction data extending to resolutions of 1.46, 1.78, and 1.57 Å, respectively. *Tv*HDX1, *Gs*HDX1, and *Rj*TsdC have the typical domain architecture for intradiol dioxygenases, comprising N-terminal (PF04444) and C- terminal (PF00775) dioxygenase domains akin to catechol dioxygenase.[52] *Tv*HDX1 and *Gs*HDX1 show a high sequence identity (72%), in contrast to *Rj*TsdC (42% and 44%, respectively). Despite this disparity, all three dioxygenases share a similar overall architecture (Figure 4B). Surprisingly, the fungal HDX1s are more structurally dissimilar to one another (RMSD values of 2.30 Å over 284 aligned residues) than when each is compared to *Rj*TsdC (1.64 Å over 268 aligned residues for *Tv*HDX1 and 1.94 Å over 269 aligned residues for *Gs*HDX1). The elevated RMSD value between the fungal enzymes is due to the different arrangement of the three α helices at the dimeric interface (Figure 4B). Nonetheless, the catalytic domains are superimposable between all three enzymes.

To gain further insight into the substrate preference, hydroxyquinol was docked into the active site of *Tv*HDX1 (Figure 4C). The active sites of all three hydroxyquinol dioxygenases contain two histidine and two tyrosine residues that coordinate the ferric ion typical of intradiol dioxygenases. In *Tv*HDX1, the side chain of Tyr212 flipped away from the ferric ion, in contrast to the metal-coordination environment depicted in *Gs*HDX1 and *Rj*TsdC. This movement of the tyrosine residue allows for the binding catechol substrate with the metal center. One notable feature in the docked model is the hydrogen bonding interaction between Asp97 with the hydroxyl group of the substrate at the fourth position, which seems to be important for proper substrate positioning. Another peculiar feature in the structure of these hydroxyquinol dioxygenases is the presence of a phospholipid at the dimer interface (Figure S17). This phospholipid is modeled as 1-heptadecanoyl-2-tridecanoyl-3-glycerol-phosphonyl choline based on the goodness of fit of the electron density. While this phospholipid is likely derived from the heterologous host *E. coli*, its presence has been observed elsewhere (for instance, in 3HB6H from *R. jostii* RHA1; PDB: 4BK1) and has been shown to be important in protein dimerization and in aiding regioselectivity control of aromatic hydroxylation.[36]

HDX1, TsdC, and related homologs, irrespective of the variation in aromatic substrate binding, are fundamentally non-heme iron catechol-1,2-dioxygenases (intradiols). The closest structural homolog for all three structures is a hydroxyquinol 1,2-dioxygenase from the bacterium *Nocardioides simplex* (PDB: 1TMX)[53] with 44%–46% sequence identity and RMSD values of 2.5, 1.7, and 1.6 Å for *Tv*HDX1, *Gs*HDX1, and *Rj*TsdC,

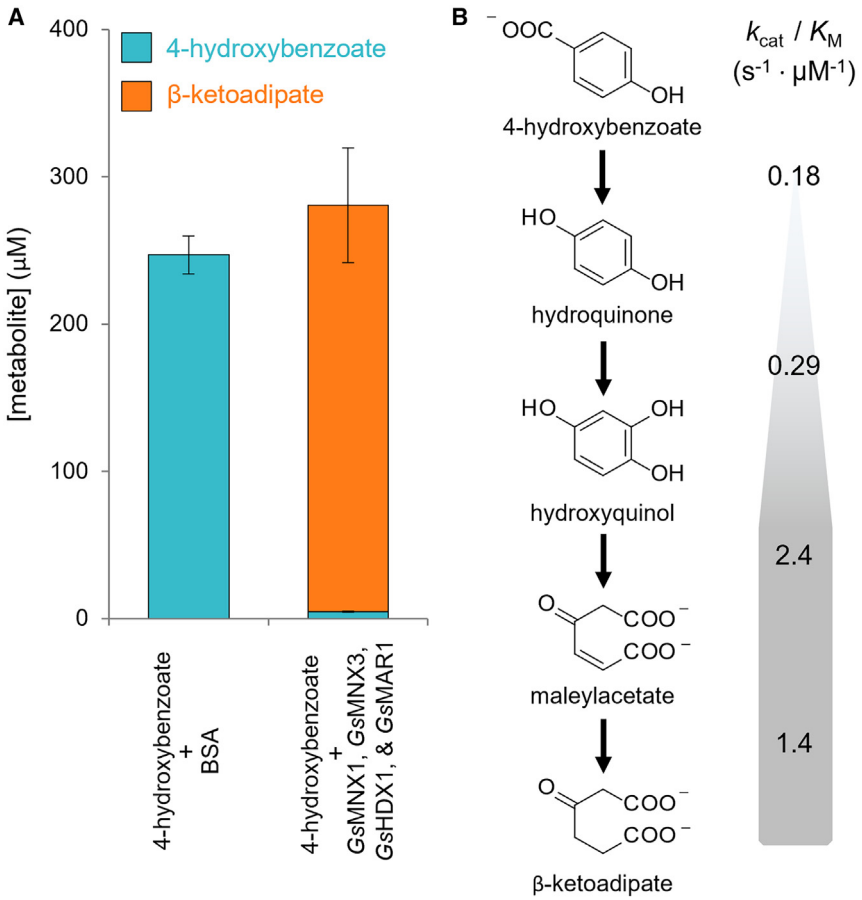

Figure 5. Cell-free conversion of 4HBA to βKA

(A) Quantification of substrate (4HBA) and product (βKA) after 16-h incubation of 4HBA with BSA, used as negative control, or with the *G. subvermispora* enzyme suite. Bars represent the average of biological triplicates, and error bars show the standard deviation of the replicates.

(B) Summary of the turnover rates shown in Table 1, corresponding to the studied enzyme cascade reaction.

respectively. Despite not containing a bound substrate, the *N. simplex* dioxygenase structure features a conserved aspartate positioned to interact with the 4-hydroxyl group of the substrate, as noted above. Another close structural homolog is a catechol 1,2-dioxygenase from the bacterium *Burkholderia ambifaria* with bound catechol (PDB: 5VXT) with 25% sequence identity with the fungal enzymes and 34% with *Rj*TsdC, and the RMSD values are 2.3, 2.9, and 2.1 Å for *Tv*HDX1, *Gs*HDX1, and *Rj*TsdC, respectively. Notably, there is no hydrogen bonding partner available to interact with the hydroxyl group of catechol in the *B. ambifaria* dioxygenase, as shown in superposition with *Tv*HDX1 (Figure 4D). The catalytic cycle on an intradiol dioxygenase initiates with the displacement of the axial metal-coordinating tyrosine and a solvent molecule to accommodate the bidentate binding of the catechol substrate to the iron center and continues as described previously (Figure S18).[54]

WRF enzymes catalyze the reduction of maleylacetate to βKA, albeit with lower catalytic efficiency compared to reported bacterial maleylacetate reductases

The last step evaluated in the hydroxyquinol pathway is the reduction of maleylacetate to βKA, which is an uncharacterized step in the fungal kingdom and is catalyzed by *Rj*TsdD (ro01858) in *R. jostii* RHA1[18] (Figure 1A). The low amino acid sequence homology between *Rj*TsdD and any WRF protein sequence has previously hindered the identification of this enzyme in WRF.[8] *In silico* structural models used in this study, generated using AlphaFold or SwissModel,[55,56] aided in the identification of putative reductases (TRAVEDRAFT_113954 and CERSUDRAFT_114286 from *T. versicolor* and *G. subvermispora*, respectively; hereafter called *Tv*MAR1 and *Gs*MAR1). In addition to the two WRF reductases, we also kinetically characterized *Rj*TsdD for comparison. Purified protein preparations of *Tv*MAR1, *Gs*MAR1, and *Rj*TsdD are colorless in appearance, and, despite their protein family name, none contain iron at appreciable level, which is consistent with prior studies where MAR1 has been shown to function independent of divalent metal ions.[57]

The kinetics assays for *Rj*TsdD and MAR1 were performed spectrophotometrically following the oxidation of NAD(P)H. Because maleylacetate is not commercially available, it was produced *in situ* from hydroxyquinol using excess of either *Rj*TsdC or *Gs*HDX1 prior to the addition of the reductase. These assays showed that *Rj*TsdD and MAR1 stoichiometrically reduced maleylacetate to βKA using NAD(P)H as the sacrificial electron donor, as determined by an HPLC-based method (Figure 5). The steady-state kinetic parameters are summarized in Table 1. Comparing the different Michaelis-Menten constants toward the nicotinamide cofactor, *Rj*TsdD utilizes both NADH and NADPH as a reducing equivalent with equal efficiency, whereas *Tv*MAR1 and *Gs*MAR1 exhibited a strong preference toward NADPH. Overall, under the conditions tested, *Rj*TsdD exhibits kinetic superiority with approximately two orders of magnitude higher catalytic efficiency compared to fungal MAR1s. This enhanced performance is primarily driven by its higher turnover frequency. *Tv*MAR1 is slightly more efficient than *Gs*MAR1, although the latter may operate better at a lower substrate concentration (Table 1).

Structural models of fungal and bacterial maleylacetate reductases provide insights into the lack of metal binding coordination compared to other reductases

*Tv*MAR1, *Gs*MAR1, and *Rj*TsdD consist of a single iron-containing dehydrogenase domain (PF00465/cd08192).[33] The structural models for the various reductases were generated *in silico* and

provided by either AlphaFold or SwissModel (Figure S19).[55,56] As mentioned previously, despite the low sequence similarity to structurally characterized MAR (24%–29% sequence identity), the overall architecture of the *Tv*MAR1 and *Gs*MAR1 matches that of MAR from bacteria such as *Agrobacterium tumefaciens* strain C58 (PDB: 3HL0), *Ralstonia eutropha* JMP134 (PDB: 3JZD), *Corynebacterium glutamicum* (PDB: 3IV7), and *Rhizobium* sp. strain MTP-10005 (also known as GraC; PDB: 3W5S)[57] with RMSD values of $\leq$1.6 Å. Structurally, MAR comprises an N-terminal Rossman fold domain and a C-terminal domain that is predominantly α helices that house the putative metal-binding site. In MAR1 and *Rj*TsdD, the putative metal-binding histidines around the active site are conserved; however, the metal-binding glutamate is substituted with asparagine in *Rj*TsdD and arginine in WRF MAR1, which likely abolishes the metal-binding coordination.

In vitro enzyme cascade for the bioconversion of 4HBA to βKA

To validate the complete hydroxyquinol pathway in WRF while simultaneously confirming the product of fungal MAR1, we tested a reaction cascade with the enzyme suite from *G. subvermispora*. In this assay, we combined 4HBA with catalytic amounts (1 μM each) of *Gs*MNX1, *Gs*MNX3, *Gs*HDX1, and *Gs*MAR1, using an excess amount NADPH, and quantified the extent of substrate depletion and βKA produced as well as any intermediate (excluding maleylacetate). After a 16-h incubation period, nearly complete conversion to βKA was achieved, with only negligible traces of 4HBA identified (Figure 5A). There was no detectable accumulation of hydroquinone or hydroxyquinol. Overall, these results validate the entire hydroxyquinol pathway in *G. subvermispora*, encompassing the conversion from 4HBA to βKA (Figure 1), and display a proof of concept for cell-free production of βKA from aromatic sources.

DISCUSSION

Despite intense study of WRF for lignin degradation, our current understanding of aromatic catabolic pathways in WRF remains limited. To that end, this study builds upon our prior systems-level study[8] and provides mechanistic clarity for each biochemical conversion step within the hydroxyquinol pathway. Additionally, it unveils the identification of maleylacetate reductases in two WRF. From a kinetics standpoint, we note a general trend of increasing catalytic efficiency for each successive step of the pathway in *G. subvermispora*, culminating at hydroxyquinol ring cleavage (Figures 5B; Table 1). The most prominent increase in catalytic efficiency, of approximately an order of magnitude, was observed between the activities of *Gs*MNX3 and *Gs*HDX1, likely to prevent accumulation of unstable and toxic hydroxyquinol.[58] Our crystallographic models offer further insights into the active-site architecture of FPMOs and non-heme iron dioxygenases, which informs common substrate activation strategies. In FPMO, substrate activation proceeds through the deprotonation of the phenolic group by a base catalyst; then, the immediate proximity of the flavin -hydroxyperoxide to the reactive carbon center specifies where the hydroxylation (or an ensuing decarboxylation) occurs (Figures S4 and S6). In non-heme iron dioxygenases, the bidentate substrate binding to the metal center anchors the reaction coordinate for the successive ring-opening additions of oxygen atoms (Figure S18). Last, our findings suggest that relying solely on structure and active-site homology may result in inaccurate substrate specificity predictions in FPMOs. Therefore, an approach that combines phylogenetic analyses of biochemically characterized fungal and bacterial enzymes (Text S2; Figure S14; Data S1) with structural biology is recommended for more reliable activity predictions of aromatic compounds, particularly in cases where enzyme assays are not feasible.

The activity of the oxidative decarboxylase GsMNX1 toward aromatic catabolic intermediates (i.e., protocatechuate) or lignin-related compounds (i.e., vanillate) beyond 4HBA suggests the existence of interconnected catabolic pathways within WRF that have yet to be fully elucidated. The higher catalytic efficiency of *Gs*MNX1 toward protocatechuate, when compared to 4HBA, implies that the hydroxylation of 4HBA to protocatechuate (a reaction that is still hypothetical) may represent a significant catabolic route for aromatic compounds in WRF. FPMOs homologous to bacterial PobA or PraI (Figure 1) appear to be missing in *G. subvermispora* or *T. versicolor*. Thus, this catabolic step may instead be catalyzed by a PhhA-like FPMO or cytochrome P450, as described previously for the filamentous fungus *Cochliobolus lunatus*.[59] Regarding vanillate, the MNX1-like reactivity in generating 2-methoxyhydroquinone (Figure 1B) was reported in 1988 in supernatants of the WRF *P. chrysosporium*. However, this activity was not linked to any specific enzyme, and kinetics were not measured.[60] In general, the catabolism of methoxylated phenolics in WRF remains poorly understood. Both *G. subvermispora* and *T. versicolor* appear to lack the conventional aerobic aromatic demethylation system, such as the Rieske-, cytochrome P450-, or tetrahydrofolate-type aromatic demethylation systems.[8,61] However, a recent studies of the filamentous fungi *Aspergillus niger* and *P. chrysosporium* have postulated a catabolic route for ring opening of 2-methoxyhydroquinone by a dioxygenase, which obviates the need for the conversion of a guaiacyl to a catechyl group prior to ring opening,[62,63] presenting a different pathway for vanillate conversion. While our study is primarily focused on a compound that exhibits the *p*-coumaryl ring substitution pattern (i.e., no methoxy groups on the aromatic ring) in lignin, future work will aim to uncover novel pathways for the conversion of G- and S-type monomers in lignin-degrading WRF.

From a systems-level perspective, reaction uncoupling events (futile cycling) exhibited by oxygenases on certain lignin-related aromatic compounds may be a beneficial feature of the biological system. For instance, MNX3 showed severe reaction uncoupling in the presence of catechol and phenol (Figure S6). This behavior has also been observed previously in Rieske-type oxygenases, such as vanillate *O*-demethylase and guaiacol *O*-demethylase, where uncoupling was noted when these systems were subjected to S-type lignin monomers.[64,65] Reaction uncoupling with these oxygenases may serve to generate H_2O_2, fueling WRF peroxidases involved in lignin degradation processes,[1] or to produce O_2 in conjunction with catalases for hydroxylation or ring-opening reactions.

The reason why WRF evolved the hydroxyquinol pathway instead of adopting the conventional βKA pathway used by bacteria remains an open question, especially given that, as described above, the last aromatic compound before ring cleavage, hydroxyquinol, is relatively unstable—it readily oxidizes under aqueous oxygenated conditions at pH 7[58]—in contrast to the stability exhibited by protocatechuate and catechol (Figure 1). The scope of the current study is limited to the *in vitro* characterization of selected enzymes within the hydroxyquinol pathway. Nevertheless, transferring the βKA and hydroxyquinol pathways to an *in vivo* context may potentially reveal advantages in actual wood decay processes. Yet, assessing these queries in WRF remains a challenge due to the absence of efficient genetic tools for these organisms and the potential redundancy of enzymes with similar activities. Indeed, based on the phylogenetic analyses of FPMOs (Figure S14), the previously reported insoluble MNX1-like CERSUDRAFT_119636 might also harbor the same activity as GsMNX1. Going forward, future research will necessitate different expression systems (e.g., *Pichia pastoris* or cell free systems) to support the redundancy hypothesis.

From an application standpoint, the hydroxyquinol pathway requires one less enzyme than the conventional βKA pathway to transform 4HBA to βKA—a high-value building block.[12,28,51] This feature holds promise for applications in cell-free conversion processes. For instance, the catabolic intermediate hydroquinone is a byproduct of various processes, including pharmaceuticals,[66] which offers an opportunity for the valorization of waste streams containing this aromatic compound. Furthermore, these findings are of paramount importance for the development of more efficient enzymatic or microbial biocatalysts aimed at producing chemicals from lignin-related aromatic compounds, specially within the context of lignin valorization.[26,27] In terms of cofactors, the hydroxyquinol pathway (from 4HBA to βKA) requires one additional molar equivalent of NAD(P)H compared to the βKA pathway (Figure 1), potentially influencing the cost of cell-free systems. Thus, weighing the cost of cofactors and the expenses associated with producing an additional enzyme would be required. Furthermore, enzymes in the hydroxyquinol pathway in WRF, including the FPMOs and the maleylacetate reductase, exhibit a preference toward NADPH. Consequently, if these fungal pathways are translated to other organisms, then additional considerations, such as a cofactor regeneration system, would be essential to maintain cellular redox balance. Overall, the validation of the hydroxyquinol pathway in WRF and the characterization of enzymes involved in its various catabolic steps represent an advancement toward a more comprehensive understanding of global carbon cycling and carbon sequestration from lignin-related compounds in fungal biomass in nature.

Limitations of the study

This study uncovers a specific enzymatic pathway for the conversion of 4HBA to βKA in WRF. However, as described above, 4HBA may also undergo hydroxylation to form protocatechuate, a pathway not addressed in this study. Additionally, gene redundancy is highly likely in WRF. Thus, we may be missing enzymes that conduct similar reactions *in vivo*, which would need to be considered if engineering aromatic catabolic pathways in WRF. Finally, we are using *E. coli* as a host for enzyme production, which does not glycosylate enzymes as fungi do, potentially altering some kinetics. Nevertheless, these enzymatic reactions could still be transferred to bacteria for other applications, making the kinetics data relevant.

RESOURCE AVAILABILITY

Lead contact

Requests for further information, resources, and reagents should be directed to and will be fulfilled by the lead contact, Davinia Salvachúa (davinia.salvachua@nrel.gov).

Materials availability

Genetic expression constructs generated in this study are available upon request.

Data and code availability

- The atomic coordinates and structure factors have been deposited in the Protein Data Bank (https://www.rcsb.org/) (PDB: 8R2T, 8R2U, 8R2V, 8R2W, and 8R2X). The deposited data will be made publicly accessible by the paper's publication date.
- This paper does not report original code.
- Any additional information required to reanalyze the data reported in this paper is available from the lead contact upon request.

ACKNOWLEDGMENTS

This material is based upon work supported by the US Department of Energy, Office of Science, Office of Biological and Environmental Research (BER) under the Early Career Award Program. This work was authored by the National Renewable Energy Laboratory, operated by Alliance for Sustainable Energy, LLC, for the US Department of Energy (DOE) under contract DE-AC36-08GO28308. The views expressed in the article do not necessarily represent the views of the DOE or the US Government. The US Government retains and the publisher, by accepting the article for publication, acknowledges that the US Government retains a nonexclusive, paid-up, irrevocable, worldwide license to publish or reproduce the published form of this work, or allow others to do so, for US Government purposes. Erika Erickson and Allison Yaguchi are thanked for the construction of pEE and pAY plasmids, respectively. The US Department of Energy Joint Genome Institute is thanked for DNA synthesis and plasmid construction of fungal oxidative decarboxylases, hydroxylases, and dioxygenases, which have been reported in a previous publication.[8] The work conducted by the US Department of Energy Joint Genome Institute (https://ror.org/04xm1d337), a DOE Office of Science User Facility, is supported by the Office of Science of the US Department of Energy operated under contract DE-AC02-05CH11231. We thank Diamond Light Source (Didcot, UK) for beamtime (proposal MX-23269) and the beamline staff at I03 and I04 for support. M.Z., P.A.C., and A.R.P. acknowledge Research England for E3 funding. K.T. is a recipient of a PhD studentship from the South Coast Biosciences Doctoral Training Partnership (SoCoBio DTP) funded by BBSRC South Coast Biosciences Doctoral Training Partnership (BB/T008768/1). Gregg T. Beckham and John E. McGeehan are thanked for their careful reading of the manuscript.

AUTHOR CONTRIBUTIONS

Conceptualization, D.S.; methodology, E.K., M.Z., K.T., and K.J.R.; investigation, E.K., A.S., Z.A.K., M.Z., K.T., M.A.I., and S.P.W.; writing – original draft, E.K., and A.S.; writing – review & editing, E.K., A.S., M.Z., and D.S.; supervision, P.A.C., A.R.P., and D.S.

DECLARATION OF INTERESTS

The authors declare no competing interests.

STAR★METHODS

Detailed methods are provided in the online version of this paper and include the following:

- KEY RESOURCES TABLE
- EXPERIMENTAL MODEL AND STUDY PARTICIPANT DETAILS
  - Bacterial strain
- METHOD DETAILS
  - Cloning
  - Protein production and purification
  - Kinetic assays
  - Enzyme assays for the quantification of substrate utilization and product validation via HPLC
- QUANTIFICATION AND STATISTICAL ANALYSIS
  - HPLC methods

SUPPLEMENTAL INFORMATION

Supplemental information can be found online at https://doi.org/10.1016/j.celrep.2024.115002.

Received: May 17, 2024
Revised: September 15, 2024
Accepted: November 6, 2024
Published: November 26, 2024

REFERENCES

1. Floudas, D., Binder, M., Riley, R., Barry, K., Blanchette, R.A., Henrissat, B., Martínez, A.T., Otillar, R., Spatafora, J.W., Yadav, J.S., et al. (2012). The Paleozoic origin of enzymatic lignin decomposition reconstructed from 31 fungal genomes. Science (New York, N.Y.) *336*, 1715–1719. https://doi.org/10.1126/science.1221748.
2. Boerjan, W., Ralph, J., and Baucher, M. (2003). Lignin biosynthesis. Annu. Rev. Plant Biol. *54*, 519–546. https://doi.org/10.1146/annurev.arplant.54.031902.134938.
3. Martínez, A.T., Speranza, M., Ruiz-Dueñas, F.J., Ferreira, P., Camarero, S., Guillén, F., Martínez, M.J., Gutiérrez, A., and del Río, J.C. (2005). Biodegradation of lignocellulosics: microbial, chemical, and enzymatic aspects of the fungal attack of lignin. Int. Microbiol. *8*, 195–204.
4. Bugg, T.D.H., Ahmad, M., Hardiman, E.M., and Rahmanpour, R. (2011). Pathways for degradation of lignin in bacteria and fungi. Nat. Prod. Rep. *28*, 1883–1896. https://doi.org/10.1039/c1np00042j.
5. Kamimura, N., Takahashi, K., Mori, K., Araki, T., Fujita, M., Higuchi, Y., and Masai, E. (2017). Bacterial catabolism of lignin-derived aromatics: New findings in a recent decade: Update on bacterial lignin catabolism. Environ. Microbiol. Rep. *9*, 679–705. https://doi.org/10.1111/1758-2229.12597.
6. Camarero, S., Bockle, B., Martinez, M.J., and Martinez, A.T. (1996). Manganese-mediated lignin degradation by *Pleurotus pulmonarius*. Appl. Environ. Microbiol. *62*, 1070–1072. https://doi.org/10.1128/aem.62.3.1070-1072.1996.
7. Perez, J., and Jeffries, T.W. (1990). Mineralization of C-Ring-Labeled Synthetic Lignin Correlates with the Production of Lignin Peroxidase, not of Manganese Peroxidase or Laccase. Appl. Environ. Microbiol. *56*, 1806–1812. https://doi.org/10.1128/aem.56.6.1806-1812.1990.
8. Del Cerro, C., Erickson, E., Dong, T., Wong, A.R., Eder, E.K., Purvine, S.O., Mitchell, H.D., Weitz, K.K., Markillie, L.M., Burnet, M.C., et al. (2021). Intracellular pathways for lignin catabolism in white-rot fungi. Proc. Natl. Acad. Sci. USA *118*, e2017381118. https://doi.org/10.1073/pnas.2017381118.
9. Schutyser, W., Renders, T., Van den Bosch, S., Koelewijn, S.F., Beckham, G.T., and Sels, B.F. (2018). Chemicals from lignin: an interplay of lignocellulose fractionation, depolymerisation, and upgrading. Chem. Soc. Rev. *47*, 852–908. https://doi.org/10.1039/C7CS00566K.
10. Lu, F., Ralph, J., Morreel, K., Messens, E., and Boerjan, W. (2004). Preparation and relevance of a cross-coupling product between sinapyl alcohol and sinapyl p-hydroxybenzoate. Org. Biomol. Chem. *2*, 2888–2890. https://doi.org/10.1039/B411428K.
11. Lu, F., Karlen, S.D., Regner, M., Kim, H., Ralph, S.A., Sun, R.C., Kuroda, K.i., Augustin, M.A., Mawson, R., Sabarez, H., et al. (2015). Naturally *p*-hydroxybenzoylated lignins in palms. BioEnergy Res. *8*, 934–952. https://doi.org/10.1007/s12155-015-9583-4.
12. Harwood, C.S., and Parales, R.E. (1996). The β-ketoadipate pathway and the biology of self-identity. Annu. Rev. Microbiol. *50*, 553–590. https://doi.org/10.1146/annurev.micro.50.1.553.
13. Ornston, L.N., and Parke, D. (1977). Curr. Top. Cell Regul. *12*, 209–262.
14. Spence, E.M., Scott, H.T., Dumond, L., Calvo-Bado, L., di Monaco, S., Williamson, J.J., Persinoti, G.F., Squina, F.M., and Bugg, T.D.H. (2020). The hydroxyquinol degradation pathway in *Rhodococcus jostii* RHA1 and *Agrobacterium* species is an alternative pathway for degradation of protocatechuic acid and lignin fragments. Appl. Environ. Microbiol. *86*, e01561-20. https://doi.org/10.1128/aem.01561-20.
15. Holesova, Z., Jakubkova, M., Zavadiakova, I., Zeman, I., Tomaska, L., and Nosek, J. (2011). Gentisate and 3-oxoadipate pathways in the yeast *Candida parapsilosis*: identification and functional analysis of the genes coding for 3-hydroxybenzoate 6-hydroxylase and 4-hydroxybenzoate 1-hydroxylase. Microbiol. *157*, 2152–2163. https://doi.org/10.1099/mic.0.048215-0.
16. Morya, R., Salvachúa, D., and Thakur, I.S.B. (2020). An untapped but promising bacterial genus for the conversion of aromatic compounds. Trends Biotechnol. *38*, 963–975. https://doi.org/10.1016/j.tibtech.2020.02.008.
17. Kitagawa, W., Kimura, N., and Kamagata, Y. (2004). A novel *p*-nitrophenol degradation gene cluster from a Gram-positive bacterium, *Rhodococcus opacus* SAO101. J. Bacteriol. *186*, 4894–4902. https://doi.org/10.1128/jb.186.15.4894-4902.2004.
18. Kasai, D., Araki, N., Motoi, K., Yoshikawa, S., Iino, T., Imai, S., Masai, E., and Fukuda, M. (2015). γ-Resorcylate catabolic-pathway genes in the soil actinomycete *Rhodococcus jostii* RHA1. Appl. Environ. Microbiol. *81*, 7656–7665. https://doi.org/10.1128/aem.02422-15.
19. Tóth, R., Nosek, J., Mora-Montes, H.M., Gabaldon, T., Bliss, J.M., Nosanchuk, J.D., Turner, S.A., Butler, G., Vágvölgyi, C., Gácser, A., et al. (2019). *Candida parapsilosis*: from genes to the bedside. Clin. Microbiol. Rev. *32*, e00111-18. https://doi.org/10.1128/cmr.00111-00118.
20. Eppink, M.H., Boeren, S.A., Vervoort, J., and van Berkel, W.J. (1997). Purification and properties of 4-hydroxybenzoate 1-hydroxylase (decarboxylating), a novel flavin adenine dinucleotide-dependent monooxygenase from *Candida parapsilosis* CBS604. J. Bacteriol. *179*, 6680–6687. https://doi.org/10.1128/jb.179.21.6680-6687.1997.
21. Eppink, M.H., Cammaart, E., Van Wassenaar, D., Middelhoven, W.J., and van Berkel, W.J. (2000). Purification and properties of hydroquinone hydroxylase, a FAD-dependent monooxygenase involved in the catabolism of 4-hydroxybenzoate in *Candida parapsilosis* CBS604. Eur. J. Biochem. *267*, 6832–6840. https://doi.org/10.1046/j.1432-1033.2000.01783.x.
22. Lubbers, R.J.M., Dilokpimol, A., Visser, J., Mäkelä, M.R., Hildén, K.S., and de Vries, R.P. (2019). A comparison between the homocyclic aromatic metabolic pathways from plant-derived compounds by bacteria and fungi. Biotechnol. Adv. *37*, 107396. https://doi.org/10.1016/j.biotechadv.2019.05.002.
23. Suzuki, H., Mori, R., Kato, M., and Shimizu, M. (2023). Biochemical characterization of hydroquinone hydroxylase from *Phanerochaete chrysosporium*. J. Biosci. Bioeng. *135*, 17–24. https://doi.org/10.1016/j.jbiosc.2022.10.001.
24. Rieble, S., Joshi, D.K., and Gold, M.H. (1994). Purification and characterization of a 1,2,4-trihydroxybenzene 1,2-dioxygenase from the basidiomycete Phanerochaete chrysosporium. J. Bacteriol. *176*, 4838–4844. https://doi.org/10.1128/jb.176.16.4838-4844.1994.

25. Kato, H., Furusawa, T.T., and Mori, R. (2022). Characterization of two 1,2,4-trihydroxybenzene 1,2-dioxygenases from *Phanerochaete chrysosporium*. Appl Microbiol Biotechnol. *106*, 4499–4509. https://doi.org/10.1007/s00253-022-12007-9.

26. Beckham, G.T., Johnson, C.W., Karp, E.M., Salvachúa, D., and Vardon, D.R. (2016). Opportunities and challenges in biological lignin valorization. Curr. Opin. Biotechnol. *42*, 40–53. https://doi.org/10.1016/j.copbio.2016.02.030.

27. Ragauskas, A.J., Beckham, G.T., Biddy, M.J., Chandra, R., Chen, F., Davis, M.F., Davison, B.H., Dixon, R.A., Gilna, P., Keller, M., et al. (2014). Lignin valorization: improving lignin processing in the biorefinery. Science *344*, 1246843. https://doi.org/10.1126/science.1246843.

28. Johnson, C.W., Salvachúa, D., Rorrer, N.A., Black, B.A., Vardon, D.R., St. John, P.C., Cleveland, N.S., Dominick, G., Elmore, J.R., Grundl, N., et al. (2019). Innovative Chemicals and Materials from Bacterial Aromatic Catabolic Pathways. Joule *3*, 1523–1537. https://doi.org/10.1016/j.joule.2019.05.011.

29. Werner, A.Z., Cordell, W.T., Lahive, C.W., Klein, B.C., Singer, C.A., Tan, E.C.D., Ingraham, M.A., Ramirez, K.J., Kim, D.H., Pedersen, J.N., et al. (2023). Lignin conversion to β-ketoadipic acid by *Pseudomonas putida* via metabolic engineering and bioprocess development. Sci. Adv. *9*, eadj0053. https://doi.org/10.1126/sciadv.adj0053.

30. Entsch, B., Cole, L.J., and Ballou, D.P. (2005). Protein dynamics and electrostatics in the function of p-hydroxybenzoate hydroxylase. Arch. Biochem. Biophys. *433*, 297–311. https://doi.org/10.1016/j.abb.2004.09.029.

31. Paul, C.E., Eggerichs, D., Westphal, A.H., Tischler, D., and van Berkel, W.J.H. (2021). Flavoprotein monooxygenases: Versatile biocatalysts. Biotechnol. Adv. *51*, 107712. https://doi.org/10.1016/j.biotechadv.2021.107712.

32. Westphal, A.H., Tischler, D., Heinke, F., Hofmann, S., Gröning, J.A.D., Labudde, D., and van Berkel, W.J.H. (2018). Pyridine nucleotide coenzyme specificity of *p*-hydroxybenzoate hydroxylase and related flavoprotein monooxygenases. Front. Microbiol. *9*, 3050. https://doi.org/10.3389/fmicb.2018.03050.

33. Mistry, J., Chuguransky, S., Williams, L., Qureshi, M., Salazar, G.A., Sonnhammer, E.L.L., Tosatto, S.C.E., Paladin, L., Raj, S., Richardson, L.J., et al. (2021). Pfam: The protein families database in 2021. Nucleic Acids Res. *49*, D412–D419. https://doi.org/10.1093/nar/gkaa913.

34. van Berkel, W.J., Eppink, M.H., and Schreuder, H.A. (1994). Crystal structure of *p*-hydroxybenzoate hydroxylase reconstituted with the modified FAD present in alcohol oxidase from methylotrophic yeasts: evidence for an arabinoflavin. Protein Sci. *3*, 2245–2253. https://doi.org/10.1002/pro.5560031210.

35. Ortiz-Maldonado, M., Gatti, D., Ballou, D.P., and Massey, V. (1999). Structure-function correlations of the reaction of reduced nicotinamide analogues with *p*-hydroxybenzoate hydroxylase substituted with a series of 8-substituted flavins. Biochemistry *38*, 16636–16647. https://doi.org/10.1021/bi991603u.

36. Montersino, S., Orru, R., Barendregt, A., Westphal, A.H., van Duijn, E., Mattevi, A., and van Berkel, W.J.H. (2013). Crystal structure of 3-hydroxybenzoate 6-hydroxylase uncovers lipid-assisted flavoprotein strategy for regioselective aromatic hydroxylation. J. Biol. Chem. *288*, 26235–26245. https://doi.org/10.1074/jbc.M113.479303.

37. Hicks, K.A., Yuen, M.E., Zhen, W.F., Gerwig, T.J., Story, R.W., Kopp, M.C., and Snider, M.J. (2016). Structural and biochemical characterization of 6-hydroxynicotinic acid 3-monooxygenase, a novel decarboxylative hydroxylase Involved in aerobic nicotinate degradation. Biochemistry *55*, 3432–3446. https://doi.org/10.1021/acs.biochem.6b00105.

38. Nakamoto, K.D., Perkins, S.W., Campbell, R.G., Bauerle, M.R., Gerwig, T.J., Gerislioglu, S., Wesdemiotis, C., Anderson, M.A., Hicks, K.A., and Snider, M.J. (2019). Mechanism of 6-hydroxynicotinate 3-monooxygenase, a flavin-dependent decarboxylative hydroxylase involved in bacterial nicotinic acid degradation. Biochemistry *58*, 1751–1763. https://doi.org/10.1021/acs.biochem.8b00969.

39. Holmgren, A. (1985). THIOREDOXIN. Annu. Rev. Biochem. *54*, 237–271. https://doi.org/10.1146/annurev.bi.54.070185.001321.

40. Martin, J.L. (1995). Thioredoxin - a fold for all reasons. Structure *3*, 245–250. https://doi.org/10.1016/S0969-2126(01)00154-X.

41. Krissinel, E., and Henrick, K. (2007). Inference of macromolecular assemblies from crystalline state. J. Mol. Biol. *372*, 774–797. https://doi.org/10.1016/j.jmb.2007.05.022.

42. Kuatsjah, E., Johnson, C.W., Salvachúa, D., Werner, A.Z., Zahn, M., Szostkiewicz, C.J., Singer, C.A., Dominick, G., Okekeogbu, I., Haugen, S.J., et al. (2022). Debottlenecking 4-hydroxybenzoate hydroxylation in *Pseudomonas putida* KT2440 improves muconate productivity from *p*-coumarate. Metab. Eng. *70*, 31–42. https://doi.org/10.1016/j.ymben.2021.12.010.

43. Enroth, C. (2003). High-resolution structure of phenol hydroxylase and correction of sequence errors. Acta Crystallogr. D *59*, 1597–1602. https://doi.org/10.1107/S0907444903014902.

44. Lubbers, R.J.M., Dilokpimol, A., Peng, M., Visser, J., Mäkelä, M.R., Hildén, K.S., and de Vries, R.P. (2019). Discovery of Novel p-Hydroxybenzoate-m-hydroxylase, Protocatechuate 3,4 Ring-Cleavage Dioxygenase, and Hydroxyquinol 1,2 Ring-Cleavage Dioxygenase from the Filamentous Fungus *Aspergillus niger*. ACS Sustain. Chem. Eng. *7*, 19081–19089. https://doi.org/10.1021/acssuschemeng.9b04918.

45. Hiromoto, T., Fujiwara, S., Hosokawa, K., and Yamaguchi, H. (2006). Crystal structure of 3-hydroxybenzoate hydroxylase from Comamonas testosteroni has a large tunnel for substrate and oxygen access to the active site. J. Mol. Biol. *364*, 878–896. https://doi.org/10.1016/j.jmb.2006.09.031.

46. Chang, H.K., and Zylstra, G.J. (2008). Examination and expansion of the substrate range of m-hydroxybenzoate hydroxylase. Biochem. Biophys. Res. Commun. *371*, 149–153. https://doi.org/10.1016/j.bbrc.2008.04.032.

47. Montersino, S., Tischler, D., Gassner, G.T., and van Berkel, W.J.H. (2011). Catalytic and structural features of flavoprotein hydroxylases and epoxidases. Adv. Synth. Catal. *353*, 2301–2319. https://doi.org/10.1002/adsc.201100384.

48. Cole, L.J., Entsch, B., Ortiz-Maldonado, M., and Ballou, D.P. (2005). Properties of *p*-hydroxybenzoate hydroxylase when stabilized in its open conformation. Biochemistry *44*, 14807–14817. https://doi.org/10.1021/bi0512142.

49. Pau, M.Y.M., Lipscomb, J.D., and Solomon, E.I. (2007). Substrate activation for O_2 reactions by oxidized metal centers in biology. Proc. Natl. Acad. Sci. USA *104*, 18355–18362. https://doi.org/10.1073/pnas.0704191104.

50. Furukawa, K., and Miyazaki, T. (1986). Cloning of a gene cluster encoding biphenyl and chlorobiphenyl degradation in Pseudomonas pseudoalcaligenes. J. Bacteriol. *166*, 392–398. https://doi.org/10.1128/jb.166.2.392-398.1986.

51. Rorrer, N.A., Notonier, S.F., Knott, B.C., Black, B.A., Singh, A., Nicholson, S.R., Kinchin, C.P., Schmidt, G.P., Carpenter, A.C., Ramirez, K.J., et al. (2022). Production of β-ketoadipic acid from glucose in *Pseudomonas putida* KT2440 for use in performance-advantaged nylons. Cell Rep. Phys. Sci. *3*, 100840. https://doi.org/10.1016/j.xcrp.2022.100840.

52. Paysan-Lafosse, T., Blum, M., Chuguransky, S., Grego, T., Pinto, B.L., Salazar, G.A., Bileschi, M.L., Bork, P., Bridge, A., Colwell, L., et al. (2023). InterPro in 2022. Nucleic Acids Res. *51*, D418–D427. https://doi.org/10.1093/nar/gkac993.

53. Ferraroni, M., Seifert, J., Travkin, V.M., Thiel, M., Kaschabek, S., Scozzafava, A., Golovleva, L., Schlömann, M., and Briganti, F. (2005). Crystal structure of the hydroxyquinol 1,2-dioxygenase from *Nocardioides simplex* 3E, a key enzyme involved in polychlorinated aromatics biodegradation. J. Biol. Chem. *280*, 21144–21154. https://doi.org/10.1074/jbc.M500666200.

54. Knoot, C.J., Purpero, V.M., and Lipscomb, J.D. (2015). Crystal structures of alkylperoxo and anhydride intermediates in an intradiol ring-cleaving

dioxygenase. Proc. Natl. Acad. Sci. USA *112*, 388–393. https://doi.org/10.1073/pnas.1419118112.

55. Waterhouse, A., Bertoni, M., Bienert, S., Studer, G., Tauriello, G., Gumienny, R., Heer, F.T., de Beer, T.A.P., Rempfer, C., Bordoli, L., et al. (2018). SWISS-MODEL: Homology modelling of protein structures and complexes. Nucleic Acids Res. *46*, W296–W303. https://doi.org/10.1093/nar/gky427.
56. Jumper, J., Evans, R., Pritzel, A., Green, T., Figurnov, M., Ronneberger, O., Tunyasuvunakool, K., Bates, R., Žídek, A., Potapenko, A., et al. (2021). Highly accurate protein structure prediction with AlphaFold. Nature *596*, 583–589. https://doi.org/10.1038/s41586-021-03819-2.
57. Fujii, T., Sato, A., Okamoto, Y., Yamauchi, T., Kato, S., Yoshida, M., Oikawa, T., and Hata, Y. (2016). The crystal structure of maleylacetate reductase from *Rhizobium* sp. strain MTP-10005 provides insights into the reaction mechanism of enzymes in its original family. Proteins *84*, 1029–1042. https://doi.org/10.1002/prot.25046.
58. Randolph, C., Lahive, C.W., Sami, S., Havenith, R.W.A., Heeres, H.J., and Deuss, P.J. (2018). Biobased chemicals: 1,2,4-benzenetriol, selective deuteration and dimerization to bifunctional aromatic compounds. Org. Process Res. Dev. *22*, 1663–1671. https://doi.org/10.1021/acs.oprd.8b00303.
59. Lah, L., Podobnik, B., Novak, M., Korošec, B., Berne, S., Vogelsang, M., Kraševec, N., Zupanec, N., Stojan, J., Bohlmann, J., and Komel, R. (2011). The versatility of the fungal cytochrome P450 monooxygenase system is instrumental in xenobiotic detoxification. Mol. Microbiol. *81*, 1374–1389. https://doi.org/10.1111/j.1365-2958.2011.07772.x.
60. Buswell, J.A., and Eriksson, K.E. (1988). Vanillate hydroxylase from Sporotrichum pulverulentum. Methods Enzymol. *161*, 274–281.
61. Erickson, E., Bleem, A., Kuatsjah, E., Werner, A.Z., DuBois, J.L., McGeehan, J.E., Eltis, L.D., and Beckham, G.T. (2022). Critical enzyme reactions in aromatic catabolism for microbial lignin conversion. Nat. Catal. *5*, 86–98. https://doi.org/10.1038/s41929-022-00747-w.
62. Kato, H., Takahashi, Y., Suzuki, H., Ohashi, K., Kawashima, R., Nakamura, K., Sakai, K., Hori, C., Takasuka, T.E., Kato, M., and Shimizu, M. (2024). Identification and characterization of methoxy- and dimethoxyhydroquinone 1,2-dioxygenase from *Phanerochaete chrysosporium*. Appl. Environ. Microbiol. *90*, 01753233–e201723. https://doi.org/10.1128/aem.01753-23.
63. Lubbers, R.J.M., Dilokpimol, A., Nousiainen, P.A., Cioc, R.C., Visser, J., Bruijnincx, P.C.A., and de Vries, R.P. (2021). Vanillic acid and methoxyhydroquinone production from guaiacyl units and related aromatic compounds using *Aspergillus niger* cell factories. Microb. Cell Factories *20*, 151. https://doi.org/10.1186/s12934-021-01643-x.
64. Bleem, A., Kuatsjah, E., Presley, G.N., Hinchen, D.J., Zahn, M., Garcia, D.C., Michener, W.E., König, G., Tornesakis, K., Allemann, M.N., et al. (2022). Discovery, characterization, and metabolic engineering of Rieske non-heme iron monooxygenases for guaiacol O-demethylation. Chem Catal. *2*, 1989–2011. https://doi.org/10.1016/j.checat.2022.04.019.
65. Notonier, S., Werner, A.Z., Kuatsjah, E., Dumalo, L., Abraham, P.E., Hatmaker, E.A., Hoyt, C.B., Amore, A., Ramirez, K.J., Woodworth, S.P., et al. (2021). Metabolism of syringyl lignin-derived compounds in *Pseudomonas putida* enables convergent production of 2-pyrone-4,6-dicarboxylic acid. Metab. Eng. *65*, 111–122. https://doi.org/10.1016/j.ymben.2021.02.005.
66. Enguita, F.J., and Leitão, A.L. (2013). Hydroquinone: environmental pollution, toxicity, and microbial answers. BioMed Res. Int. *2013*, 542168. https://doi.org/10.1155/2013/542168.
67. (2017). STARANISO (Global Phasing Limited, United Kingdom.
68. Vagin, A., and Teplyakov, A. (2010). Molecular replacement with MOLREP. Acta Crystallogr. D Biol. Crystallogr. *66*, 22–25. https://doi.org/10.1107/s0907444909042589.
69. Emsley, P., Lohkamp, B., Scott, W.G., and Cowtan, K. (2010). Features and development of Coot. Acta Crystallogr. D Biol. Crystallogr. *66*, 486–501. https://doi.org/10.1107/s0907444910007493.
70. Murshudov, G.N., Skubák, P., Lebedev, A.A., Pannu, N.S., Steiner, R.A., Nicholls, R.A., Winn, M.D., Long, F., and Vagin, A.A. (2011). REFMAC5 for the refinement of macromolecular crystal structures. Acta Crystallogr. D Biol. Crystallogr. *67*, 355–367. https://doi.org/10.1107/s0907444911001314.
71. Williams, C.J., Headd, J.J., Moriarty, N.W., Prisant, M.G., Videau, L.L., Deis, L.N., Verma, V., Keedy, D.A., Hintze, B.J., Chen, V.B., et al. (2018). MolProbity: More and better reference data for improved all-atom structure validation. Protein Sci. *27*, 293–315. https://doi.org/10.1002/pro.3330.
72. The PyMOL Molecular Graphics System V. Version 2.0 (Schrödinger, LLC). https://pymol.org/support.html
73. McNaught, K.J., Kuatsjah, E., Zahn, M., Prates, É.T., Shao, H., Bentley, G.J., Pickford, A.R., Gruber, J.N., Hestmark, K.V., Jacobson, D.A., et al. (2023). Initiation of fatty acid biosynthesis in Pseudomonas putida KT2440. Metab. Eng. *76*, 193–203. https://doi.org/10.1016/j.ymben.2023.02.006.
74. (2023). Molecular Operating Environment (MOE) (Chemical Computing Group ULC (Canada).
75. Michener, W.E., Woodworth, S.P., Haugen, S.J., Ingraham, M.A., Ramirez, K.J., Beckham, G.T., and Salvachúa, D. (2024). White-Rot Fungi Aromatic Catabolic Intermediates Analyzed by HPLC-DAD (protocol.io).

STAR★METHODS

KEY RESOURCES TABLE

REAGENT or RESOURCE	SOURCE	IDENTIFIER
Bacterial and virus strain		
Escherichia coli BL21λ(DE3)	New England Biolabs	BL21λ(DE3)
Chemicals, peptides, and recombinant proteins		
Peroxidase from horseradish	Sigma-Aldrich	P8125-25KU
Catalase from bovine liver	Sigma-Aldrich	C9322-1g
HEPES	RPI	H75030–500.0
Sulfuric acid	Fisher	C068
LB Miller	RPI	L24400-2000.2kg
Sodium hydroxide	Fisher	S318-500g
4-hydroxybenzoate	Sigma	240141-50G
Hydrochloric acid	Sigma	258148-500ML
Tris base	RPI	T60040
FAD	Sigma	F6625
Sodium hydrosulfite	Fisher	71699-50g
Protocatechuate	Sigma	14916-25g
Vanillate	Sigma	H36001
3-hydroxybenzoate	Sigma	H20008-5g
2-hydroxybenzoate	Sigma	247006
Hydroquinone	Sigma	H17902
2-methoxyhydroquinone	Sigma	176893-5G
Hydroxyquinol	Sigma	173401-1G
Resorcinol	Sigma	307521-100G
Catechol	Sigma	PHL82372-100MG
Phenol	Sigma	1524806-500MG
Syringate	Sigma	S6881-5G
Imidazole	Sigma	12399-100G
DMSO	Fisher	472301-100mL
IPTG	Goldbio	I2481C-25
NADPH	Roche	10107824001
NADH	Roche	10128023001-1g
β-Ketoadipate	Sigma	O7753
Muconate	Sigma	15992-5G-F
Ferric sulfate heptahydrate	Sigma	F7002-250G
HMW protein standard	Cytiva	28403842
Recombinant proteins produced in this study	Information in this manuscript	Gene products from Table S1
Deposited data		
Atomic coordinates and structure factors –enzyme GsMNX1	This paper	PDB: 8R2T
Atomic coordinates and structure factors –enzyme TvMNX3	This paper	PDB: 8R2U
Atomic coordinates and structure factors –enzyme GsHDX1	This paper	PDB: 8R2V
Atomic coordinates and structure factors –enzyme TvHDX1	This paper	PDB: 8R2W

(*Continued on next page*)

Continued

REAGENT or RESOURCE	SOURCE	IDENTIFIER
Atomic coordinates and structure factors –enzyme RjTsdC	This paper	PDB: 8R2X
LC-MS/MS analysis methods	This paper	dx.doi.org/10.17504/protocols.io.n92ldmkpol5b/v1
Oligonucleotides		
Primer oEUK236 Sequence (5' → 3') GCCGCGCGGCAGCCATA TGACCACCTACTTCACCGA	This paper	N/A
Primer oEUK237 Sequence (5' → 3') GTTAGCAGCCGGATCCTCA GGAGCTGCCACG	This paper	N/A
Primer oEUK238 Sequence (5' → 3') GCCGCGCGGCAGCCATATG CGCCCGTTCGTCCACT	This paper	N/A
Primer oEUK239 Sequence (5' → 3') GTTAGCAGCCGGATCCTT ATGGGGTGCTTTCCGGG	This paper	N/A
Recombinant DNA		
Plasmids, see Table S1	This paper	N/A
Synthesized genes, see Table S2	This paper	N/A
Software and algorithms		
MS Excel	N/A	Microsoft 365
Leonora	N/A	ISBN: 019854877X
ClustalW	N/A	Clustal Omega < EMBL-EBI
iTOL	N/A	itol.embl.de
PyMOL 2.0	N/A	pymol.org
COOT	N/A	WinCoot 0.9.8.95
The Molecular Operating Environment (MOE 2022.02)	N/A	https://www.chemcomp.com/en/Download_Request.htm
STARANISO	N/A	https://staraniso.globalphasing.org/cgi-bin/staraniso.cgi
Molrep: version 11.9.02	N/A	CCP4 Cloud v.1.7.007
REFMAC5 version 5.8.0411	N/A	CCP4 Cloud v.1.7.007
MolProbity version 4.5	N/A	http://molprobity.biochem.duke.edu/
Coot: version 0.9.8.7	N/A	CCP4 Cloud v.1.7.007

EXPERIMENTAL MODEL AND STUDY PARTICIPANT DETAILS

Bacterial strain

The bacterial strain utilized for heterologous protein expression was *Escherichia coli* BL21λ(DE3). Cultivation media contained lysogeny broth (LB Miller) supplemented with 100 mg/L ampicillin or 50 mg/L kanamycin and incubation was conducted at 37°C and 200 rpm.

METHOD DETAILS

Cloning

DNA manipulation and propagation were performed using standard methods. Plasmids for heterologous expressions are listed in Table S1. DNA syntheses were performed by TWIST Biosciences and are listed in Table S2. Primers used for subcloning are listed in Table S3. Gibson Assembly master mix (NEB) was used for plasmid constructions. All of the gene numbering used for this work are based on the Mycocosm database.

Protein production and purification

All proteins used for *in vitro* assays were heterologously produced in *E. coli* BL21λ(DE3) lines transformed with appropriate pET-based expression systems (Table S1) in lysogeny broth (LB Miller) supplemented with 100 mg/L ampicillin or 50 mg/L kanamycin. An overnight starter culture (125 mL flask with 40 mL media) was used to inoculate the main culture (2.5 L flask with 1 L media) at 1% (v/v). Seed and production cultures were grown at 37 °C at 200 rpm. Upon reaching an OD_{600} of 0.7, the production culture was induced with the addition of 1 mM isopropyl ß-D-1-thiogalactopyranoside (IPTG), and the temperature lowered to 16°C. The culture was grown for an additional 16–18 h prior to harvesting by centrifugation. At the point of induction, 0.1 mM riboflavin was also added to strains producing FPMO, and 0.5 mM of ferrous sulfate was added to strains producing *Rj*TsdC or HDX1. The production of *Gs*MNX1 was also supplemented with the co-production of GroEL/ES using pGro7 (Takara) and the growth media for this *E. coli* strain was supplemented with 30 mg/L chloramphenicol and 0.5 g/L L-arabinose. The resulting biomass was frozen at −80°C until further processing.

All proteins were purified following immobilized metal ion affinity chromatography (IMAC) and anion exchange chromatography. Thawed biomass was resuspended with buffer A (20 mM HEPES, 100 mM NaCl, pH 7.5) and ∼1 mg of DNaseI prior to lysis using a French press. Cleared lysate, achieved by centrifugation and filtration through 0.45 μm filter, was applied to an IMAC resin – either Ni-Sepharose (Cytiva), NiNTA (GoldBio) or a HisTrap cartridge (Cytiva) – and washed with buffer A containing up to 20 mM imidazole. The protein was eluted with buffer A and 200 mM imidazole. The protein was concentrated and exchanged to buffer A using a 10 or 30 kDa spin column concentrator before application to a Source 15Q resin (Cytiva) operated with ÄKTA Pure fast protein liquid chromatography unit (Cytiva). The protein was eluted following a linear gradient of 1 M NaCl in buffer A. The fraction of interest was pooled, concentrated, exchanged to buffer A, frozen as beads, and stored at −80°C until further use.

Kinetic assays

General features of activity assays for oxygenases

Activity assays for the oxygenases are determined by following the consumption of the co-substrate O_2 using a Clark-type electrode OXYG1+ (Hansatech). The electrode was calibrated following the manufacturer's instruction using air-saturated water and sodium hydrosulfite. The assay was performed in a 1 mL format using air-saturated 50 mM Tris.SO_4 pH 7 operating at 25°C, 10 μM FAD. The observed enzymatic rate was corrected for the non-enzymatic background rate. The steady-state and inhibition kinetic parameters were obtained by fitting the Michaelis-Menten and mixed inhibition equations to the data.

Activity assay for GsMNX1

The *Gs*MNX1-catalyzed decarboxylating hydroxylation of 4HBA, protocatechuate, and vanillate was monitored by oxygraphy. A typical assay is performed using 0.1 μM of *Gs*MNX1. The dependency of the initial rate of *Gs*MNX1 was performed using 15.6 to 500 μM for 4HBA, protocatechuate, vanillate, and 25 to 500 μM NADPH. Negative controls were generated under the same conditions but replacing NADPH with buffer.

Coupling efficiency assay for GsMNX1

Coupling efficiency for *Gs*MNX1 was determined by oxygraphy by comparing the rates of oxidative decarboxylation of 4HBA, protocatechuate, and vanillate, in the presence or absence of 5 U of catalase (Sigma Aldrich). This assay contains 0.5 μM *Gs*MNX1, 1 mM aromatic substrate, and 0.5 mM NADPH. The lowered initial rates for catalase-supplemented reactions represent reaction uncoupling where hydrogen peroxide was unproductively produced as a by-product of NADPH-consuming O_2 reduction in the presence of the unsuitable substrates.

Activity assay for GsMNX3 and TvMNX3

The MNX3-catalyzed hydroxylation of hydroquinone and resorcinol was monitored by oxygraphy as described above. A typical assay is performed using 0.2 μM of *Tv*MNX3 or 0.5 μM of *Gs*MNX3. The dependency of the initial rate of MNX3 toward the concentration of 0–125 μM for hydroquinone, 0–1 mM for resorcinol, and 0–0.5 mM NADPH.

Coupling efficiency assay for GsMNX3 and TvMNX3

Coupling efficiency of MNX3 were determined against a substrate panel that includes phenol, catechol, resorcinol, and hydroquinone. The assay was performed using 0.5 μM of MNX3, 1 mM aromatic substrate, 0.5 mM NADPH, with or without 5 U of catalase (Sigma Aldrich) as described for *Gs*MNX1.

Inhibition assays for GsMNX3 and TvMNX3

Inhibitor screening for MNX3-catalyzed (0.5 μM) hydroxylation of hydroquinone in the presence of 4HBA, protocatechuate, vanillate, and 2-methoxyhydroquinone were monitored by oxygraphy. This assay contains 0.5 μM MNX3, 1 mM each of hydroquinone and the putative inhibitor, and 0.5 mM NADPH. Inhibition assay of MNX3-catalyzed hydroxylation of hydroquinone in the presence of 4HBA was performed by oxygraphy. This assay contains 0.15 μM *Tv*MNX3 or 0.36 μM *Tv*MNX3, 0.5 mM NADPH, 5–150 μM hydroquinone, 0–2 mM 4HBA.

Activity assays for RjTsdB

*Rj*TsdB was evaluated qualitatively as a single replicate by oxygraphy using OXYG1+ and air-saturated 50 mM Tris.SO4 pH 7, 10 μM FAD, at 25°C. In these assays each of the reagents were added sequentially as described. The reaction evaluating the ability of purified *Rj*TsdB to hydroxylate resorcinol was evaluated by monitoring the oxygen consumption upon the successive additions of 5 U catalase, 1 mM resorcinol, 2 μM *Rj*TsdB, 0.5 mM NADH, 0.5 mM NADPH, and 1 μM *Gs*MNX3. The reaction evaluating the ability of purified *Rj*TsdB to hydroxylate hydroquinone was evaluated by monitoring the oxygen consumption upon the successive additions of

1 mM hydroquinone, 2 μM *Rj*TsdB, 0.5 mM NADH, 5 U catalase, 0.5 mM NADPH, and 1 μM *Gs*MNX3. The reaction evaluating the ability of purified *Rj*TsdB to hydroxylate protocatechuate was evaluated by monitoring the oxygen consumption upon the successive additions of 2 μM *Rj*TsdB, 0.5 mM NADH, 1 mM protocatechuate, 2 μM *Rj*TsdA, 0.5 mM NADPH, and 1 μM PobA.

Activity assay for GsHDX1, TvHDX1, and RjTsdC

TsdC and HDX1-catalyzed transformation of hydroxyquinol and catechol was monitored following the consumption of O_2 as described above. The dependency of the initial rate of dioxygenase toward the concentration of hydroxyquinol and catechol was performed using 0–100 mM of the aromatic substrates and 10 or 1000 nM of dioxygenase.

Activity assay for GsMAR1, TvMAR1, and RjTsdD

The *Rj*TsdD and MAR1-catalyzed reduction of maleylacetate to βKA was monitored following the consumption of NAD(P)H at 340 nm ($\varepsilon_{340}^{NADH} = 6.2\ mM^{-1}\ cm^{-1}$) using Cary4000 UV-Vis spectrophotometer (Agilent). A typical assay was performed in 1 mL format using 1 mL quartz cuvette using air-saturated 50 mM Tris.SO_4 pH 7 and 10 nM of *Rj*TsdD or MAR1. The reaction temperature was maintained at 25°C using a Peltier device. The observed enzymatic rate was corrected for the non-enzymatic background rate. Maleylacetate was produced *in situ* using varying concentrations of hydroxyquinol and 1 μM of *Rj*TsdC/HDX1. The dependency of the initial rate of TsdD and MAR1 toward the concentration of maleylacetate was performed using 500 μM of NADPH and 0–300 μM of hydroxyquinol. The dependency of the initial rate of *Rj*TsdD/MAR1 toward the concentration of NAD(P)H was performed using 200 μM of hydroxyquinol and 0–500 μM of NAD(P)H.

Enzyme assays for the quantification of substrate utilization and product validation via HPLC

General features of activity assays

Sample preparation for HPLC-based analyses is typically performed in air-saturated 50 mM Tris.SO_4 pH 7, 10 μM FAD, and incubated at 25°C. The sample was incubated overnight and filtered through 0.22 μm filter before the chromatographic separation.

Assay for *TRAVEDRAFT_32834 gene product and* GsMNX1

Samples for product confirmation of MNX1 reactions were generated by adding 5 μM *Gs*MNX1 to 1 mM substrate (4HBA, 3-hydroxybenzoate, 2-hydroxybenzoate, vanillate, syringate, protocatechuate) in the presence of excess NADPH (750 μM) to a final volume of 1 mL. Reactions for TRAVEDRAFT_32834 gene product were performed similarly but with 2 mM aromatic substrates. Reactions were incubated for 1 h at 25°C with occasional agitation before being quenched 1:1 (v/v) with DMSO. Samples were frozen at −20°C until analysis. Negative controls were generated under the same conditions but with replacement of cofactor with buffer solution. Samples were generated in triplicate.

Assay for GsMNX3 and TvMNX3

Samples for product confirmation of MNX3 reactions were generated by adding 5 μM *Gs*MNX3 and *Tv*MNX3 to 1 mM substrate in the presence of 500 μM NADPH. Reactions were incubated for 1 h at 25°C with occasional agitation before being quenched 1:1 (v/v) with DMSO. Samples were frozen at −20°C until analysis. Negative controls were generated under the same conditions but with replacement of cofactor with buffer solution. Samples were generated in triplicate.

Assay for GsHDX1, TvHDX1, and RjTsdC

Samples for the conversion of hydroxyquinol or catechol by HDX1 or TsdC were prepared using 200 μM hydroxyquinol or 100 μM and either 0.5 μM dioxygenase or equivalent amount of BSA. Samples for the conversion of hydroxyquinol were additionally supplemented with 1 μM of *Rj*TsdD and 1 mM of NADPH. Three biological replicates were incubated for 16 h at room temperature.

Assay for cell-free chain reaction for the full pathway validation

Samples for cell free chain reaction were prepared using 250 μM 4HBA, 2 mM NADPH, and either 0.5 μM of each of *Gs*MNX1, *Gs*MNX3, *Gs*HDX1, and *Gs*MAR1, or equivalent amount of BSA (negative control). Three biological replicates were incubated for 16 h at room temperature.

Phylogenetic analyses

The FPMO phylogenetic analysis was performed using the EMBL multiple sequence alignment web server using the default setting of ClustalW algorithm and sequences listed in Supplementary Data S1. The phylogenetic tree was built using the iTOL web server using the circular settings while ignoring the branch length.

Crystallization and structure determination

For crystallization, the proteins were concentrated to 10 mg/mL and sitting drop crystallization trials were set up with a Mosquito crystallization robot (sptlabtech) using SWISSCI 3-lens low profile crystallization plates. Crystals appeared in the following conditions: (A) *Gs*MNX1: LMB screen from Molecular Dimensions condition G7 (11% PEG 8000, 0.4 M sodium chloride, 0.1 M sodium cacodylate pH 6.2). (B) *Tv*MNX3: Structure Screen 1 + 2 from Molecular Dimensions condition E12 (10% PEG 6000, 5% MPD, 0.1 M HEPES pH 7.5). (C) *Gs*HDX1: Structure Screen 1 + 2 from Molecular Dimensions condition F11 (1.6 M ammonium sulfate, 10% 1,4-dioxane, 0.1 M MES pH 6.5). (D) *Tv*HDX1: PACT screen from Molecular Dimensions condition F2 (20% PEG 3350, 0.2 M sodium bromide, 0.1 M Bis-Tris propane pH 6.5). (E) *Rj*TsdC: PACT screen from Molecular Dimensions condition C10 (20% PEG 6000, 0.2 M magnesium chloride, 0.1 M HEPES pH 7.0).

The crystals were cryo-protected with 20% glycerol in the crystallization solution and flash-frozen into liquid nitrogen. Diffraction data were collected at the Diamond Light Source (Didcot, UK) and automatically processed using STARANISO[67] on ISPyB. The structure was solved by molecular replacement with MOLREP[68] using AlphaFold structure predictions.[56] Model building was performed in Coot[69] and the structures were refined with REFMAC5.[70] MolProbity[71] was used to evaluate the final structure model

and PyMOL[72] for protein model visualization. Data and Refinement statistics are summarized in Table S4. The atomic coordinates have been deposited in the Protein DataBank and are available under the accession codes 8R2T, 8R2U, 8R2V, 8R2W, and 8R2X.

Size exclusion chromatography (SEC) analysis of TvMNX3

The in solution oligomeric state of *Tv*MNX3 was determined as described previously[73] with double the protein loading (2 mg/mL). In short, the protein was resolved isocratically on a HiLoad 16/600 Superdex 75 pg operated with an ÄKTA FPLC system (Cytiva) using 20 mM Tris-Cl, 100 mM NaCl pH 8 at room temperature. The retention time of *Tv*MNX3 were compared to the retention times of protein standards in low molecular weight gel filtration calibration kit (Cytiva).

Molecular docking

The Molecular Operating Environment (MOE) package[74] was used for substrate docking. The predicted productive conformations of 4-hydroxybenzoate in *Gs*MNX1 [Binding_mode 1 and Binding_mode 2] were modeled based on 6-hydroxynicotinate in the catalytic site of 6-hydroxynicotinate 3-monooxygenase [Binding_mode 1] and 3-hydroxybenzoate in the catalytic site of 3-hydroxybenzoate 6-hydrolase (PDB 4BK1) [Binding_mode 2]. For *Gs*MNX1 docking, chain A was selected. The selection of the receptor was based on the 'All atoms selection'. The selection of the ligand site was based on the 'Selected residues' option in Dock module in MOE, to cover the binding site. The selected residues for docking were: Met202, His211, Met213, Tyr215, Asn223, Val225, and Ala298. The number of docking iterations was adjusted to 1000. The predicted productive conformation of hydroquinone in *Tv*MNX3 was modeled based on phenol in the catalytic site of phenol hydroxylase (PDB 1FOH). The predicted productive conformations of hydroxyquinol in *Tv*HDX1, *Rj*TsdC and *Gs*HDX1 were modeled based on catechol in the catalytic site of catechol 1,2-dioxygenase (PDB 5VXT). In general, the substrates were docked using a rigid docking approach within the Dock module of MOE. The Triangle matcher algorithm was used for initial placement of substrates, with the placements being scored using the London ΔG method. The predicted productive conformations of the protein-substrate complexes were maintained using restraint energy minimizations carried out using the Amber-10 forcefield.

QUANTIFICATION AND STATISTICAL ANALYSIS

HPLC methods

Analyses of aromatic compounds and muconic acid

Muconic acid and aromatic intermediates were analyzed by HPLC using diode array detection (HPLC-DAD) as detailed in the recently published protocol deposited on protocols.io (dx.doi.org/10.17504/protocols.io.n92ldmkpol5b/v1).[75] Analytes of interest were chromatographically separated using a reverse phase C18(2) column and a gradient of aqueous 0.16% formic acid and acetonitrile. Quantitation was performed using standard curves for each individual compound.

Analysis of βKA

βKA was analyzed as described previously.[51] Briefly, βKA is hydrolyzed to levulinic acid using sulfuric acid and heat and quantified as such. Samples were analyzed using HPLC and refractive index detection with separation achieved using an Aminex HPX-87H column and an isocratic mobile phase comprised of 0.01N sulfuric acid.

Statistical details

Standard deviation was used to calculate errors within biological replicates. This information can be found in figure captions. MS excel was used to calculate standard deviation. Leonora was used to calculate best fit and standard error.